JPn Neuroscience
The Journal of Physiology

J Physiol 592.16 (2014) pp 3463–3494

Direct excitation of parvalbumin-positive interneurons by M_1 muscarinic acetylcholine receptors: roles in cellular excitability, inhibitory transmission and cognition

Feng Yi[1,2], Jackson Ball[1,2], Kurt E. Stoll[1,2], Vaishali C. Satpute[1,2,3], Samantha M. Mitchell[1,2,4], Jordan L. Pauli[1,2], Benjamin B. Holloway[1,2], April D. Johnston[1,2], Neil M. Nathanson[5], Karl Deisseroth[6], David J. Gerber[7], Susumu Tonegawa[7] and J. Josh Lawrence[1,2]

[1] *COBRE Center for Structural and Functional Neuroscience*
[2] *Department of Biomedical and Pharmaceutical Sciences*
[3] *Neuroscience Graduate Program*
[4] *Davidson Honors College, The University of Montana, Missoula, MT 59812, USA*
[5] *Department of Pharmacology, University of Washington, Box 357750 Seattle, WA 98195-7750, USA*
[6] *Department of Bioengineering, Stanford University, Stanford, CA, USA*
[7] *Howard Hughes Medical Institute, RIKEN–MIT Neuroscience Research Center, The Picower Institute for Learning and Memory, Department of Biology and Department of Brain and Cognitive Sciences, Massachusetts Institute of Technology, Cambridge, MA 02139, USA*

Key points

- Parvalbumin-containing (PV) neurons from mouse CA1 hippocampus (HC) and prefrontal cortex exhibit a fast spiking phenotype *in vitro*. Within CA1, HC PV cells are mainly comprised of basket and bistratified cell types.
- Direct activation of muscarinic acetylcholine receptors (mAChRs) enhances excitability more in CA1 HC than in prefrontal cortex PV cells.
- mAChR-induced excitation of CA1 PV cells occurs through direct activation of M_1 mAChRs.
- Transgenetic deletion of M_1 mAChRs from PV cells diminishes M_1 mAChR expression and cholinergic excitation of CA1 PV cells.
- mAChR-induced excitation exclusively in PV cells enhances GABAergic transmission in CA1 pyramidal cells.
- *In vivo* activation of M_1 mAChRs in PV cells is important in recognition and working memory but not spatial memory.

Abstract Parvalbumin-containing (PV) neurons, a major class of GABAergic interneurons, are essential circuit elements of learning networks. As levels of acetylcholine rise during active learning tasks, PV neurons become increasingly engaged in network dynamics. Conversely, impairment of either cholinergic or PV interneuron function induces learning deficits. Here, we examined PV interneurons in hippocampus (HC) and prefrontal cortex (PFC) and their modulation by muscarinic acetylcholine receptors (mAChRs). HC PV cells, visualized by crossing PV-CRE mice with Rosa26YFP mice, were anatomically identified as basket cells and PV bistratified cells in the stratum pyramidale; in stratum oriens, HC PV cells were electrophysiologically distinct from somatostatin-containing cells. With glutamatergic transmission pharmacologically blocked, mAChR activation enhanced PV cell excitability in both CA1 HC and PFC; however, CA1 HC PV cells exhibited a stronger postsynaptic depolarization than PFC PV cells. To delete M_1 mAChRs genetically from PV interneurons, we created PV-M_1 knockout mice by crossing PV-CRE and floxed M_1 mice. The elimination of M_1 mAChRs from PV cells diminished M_1 mAChR immunoreactivity and muscarinic excitation of HC PV cells. Selective cholinergic activation of HC PV interneurons using Designer Receptors Exclusively Activated by Designer Drugs technology enhanced the frequency and amplitude of inhibitory synaptic currents in CA1 pyramidal cells.

DOI: 10.1113/jphysiol.2014.275453

Finally, relative to wild-type controls, PV-M_1 knockout mice exhibited impaired novel object recognition and, to a lesser extent, impaired spatial working memory, but reference memory remained intact. Therefore, the direct activation of M_1 mAChRs on PV cells contributes to some forms of learning and memory.

(Resubmitted 4 April 2014; accepted after revision 26 May 2014; first published online 30 May 2014)
Corresponding author J. Josh Lawrence: COBRE Center for Structural and Functional Neuroscience, Department of Biomedical and Pharmaceutical Sciences, The University of Montana, Missoula, MT 59812, USA. Email: josh.lawrence@umontana.edu

Abbreviations ACh, acetylcholine; ACSF, artificial cerebrospinal fluid; ADF, afterdeflection; ADP, afterdepolarization; AHP, afterhyperpolarization; BC, basket cell; BiS, bistratified cell; CNO, clozapine N-oxide; DR, discrimination ratio; DREADD, Designer Receptors Exclusively Activated by Designer Drugs; FS, fast-spiking; HC, hippocampal; hM3Dq, human G_q-coupled M_3 receptor with ACh binding site mutated to bind clozapine N-oxide; I_{hold}, holding current; KO, knockout; M_1KO, M_1 mAChR knock out; mAChR, muscarinic acetylcholine receptor; MS–DBB, medial septum–diagonal band of Broca; MWM, Morris water maze; NOR, novel object recognition; OFM, open field maze; O-LM, oriens lacunosum-moleculare; PBS, phosphate-buffered saline; PCR, polymerase chain reaction; PFA, paraformaldehyde; PFC, prefrontal cortex; PING, pyramidal cell-interneuron gamma; PV, parvalbumin; PV BCs, PV basket cells; PV-CRE, parvalbumin-CRE; PV-M_1KO, transgenic mice in which M_1 mAChRs have been eliminated from PV cells; PV-Rosa, mice obtained from crossing PV-CRE and Rosa26YFP mice, allowing the visualization of YFP in PV cells; R_a, access resistance; R_{in}, input resistance; sIPSC, spontaneous inhibitory postsynaptic current; SOM-CRE, somatostatin-CRE; SOM-Rosa, mice obtained from crossing SOM-CRE and Rosa26YFP mice, allowing the visualization of YFP in SOM cells; SO, stratum oriens; SP, stratum pyramidale; SR, stratum radiatum; WT, wild-type; τ_m, membrane time constant.

Introduction

Cholinergic modulation of neuronal activity plays a central role in learning and cognition (Hasselmo & Sarter, 2011). Cholinergic activation of cortical and HC targets is thought to contribute to the generation of theta (Buzsáki, 2002) and gamma (Fisahn *et al.* 1998; Fellous & Sejnowski, 2000; Buzsáki & Wang, 2012) oscillations. These neuronal oscillations arise from the participation of glutamatergic principal cells and diverse subtypes of GABAergic inhibitory interneurons (Klausberger & Somogyi, 2008). Cholinergic projection neurons from the medial septum–diagonal band of Broca (MS–DBB) release acetylcholine (ACh) into the hippocampus (Fadda *et al.* 1996; Pepeu & Giovannini, 2004), profoundly amplifying the magnitude of theta oscillations (Lee *et al.* 1994). Ablation of the MS–DBB cholinergic input to the HC (Brito *et al.* 1983; Lee *et al.* 1994) or pharmacological blockade of muscarinic ACh receptors (mAChRs; Givens & Olton, 1990) reduces the magnitude of theta oscillations. The loss of cholinergic control over HC and cortical activity may also partially account for memory impairments in Alzheimer's disease (Coyle *et al.* 1983).

Cholinergically induced HC gamma oscillations *in vitro* (Fisahn *et al.* 1998; Gulyás *et al.* 2010) are eliminated in global M_1 mAChR knockout (M_1 KO) mice (Fisahn *et al.* 2002). The frequency and magnitude of gamma oscillations are thought to be determined by the net excitation of the interneurons and the kinetics of the inhibitory postsynaptic potentials (Bartos *et al.* 2007; Buzsáki & Wang, 2012). Modelling and physiological studies both indicate that excitation of parvalbumin-positive (PV) interneurons is a primary mechanism for the generation of gamma oscillations (Cardin *et al.* 2009; Sohal *et al.* 2009; Oren *et al.* 2010; Buzsáki & Wang, 2012).

Direct and synaptic mechanisms converge to control PV interneuron excitability (Bartos *et al.* 2007; Buzsáki & Wang, 2012), thereby regulating the participation of these neurons in network activity. Although strongly regulated by glutamatergic circuit mechanisms (Pouille & Scanziani, 2004), the cellular excitability of PV neurons is subject to regulation by multiple neuromodulators (Cobb & Lawrence, 2010). Specifically, mAChR activation directly depolarizes PV interneurons (Cea-del Rio *et al.* 2010; Chiang *et al.* 2010; Pafundo *et al.* 2013), an effect that is eliminated in global M_1 KO mice (Cea-del Rio *et al.* 2010). Single cell RT-PCR transcript analysis has indicated that the M_1 mAChR is the sole postsynaptic mAChR subtype present in PV basket cells (PV BCs; Cea-del Rio *et al.* 2010). Therefore, loss of M_1 mAChRs from PV cells could potentially impair the generation of gamma oscillations and contribute to, or account for, memory impairments observed in global M_1 KO mice (Anagnostaras *et al.* 2003), particularly for memory tasks that require the engagement of PV networks (Murray *et al.* 2011).

In this study, we generated homozygous PV-M_1KO mice by crossing PV-CRE and floxed M_1 mice, selectively eliminating M_1 mAChRs from PV cell types. First, we established that mAChR-induced changes in HC PV cell excitability depend on the direct activation of M_1 mAChRs. Second, mAChR activation of PV cells enhanced

inhibitory synaptic transmission on to CA1 pyramidal cells. Finally, in PV-M_1KO mice, recognition and working memory were impaired, but spatial memory remained intact. Therefore, some forms of learning require direct M_1 mAChR-mediated excitation of PV microcircuits.

Methods

Ethics statement

All procedures were performed in accordance with the University of Montana Institutional Animal Care and Use Committee (Animal Use Protocols 030–10, 026–11 and 035–13). Mice were housed together in one breeding pair per cage. After wean, mice were socially housed in gender-specific groups of four to five littermates per cage as backup breeders or experimental stock animals.

Determination of CRE zygosity

PV-CRE (Hippenmeyer *et al.* 2005; stock no. 008069; Jackson Labs, Bar Harbor, ME, USA) and somatostatin-CRE (SOM-CRE; stock no. 013044; Jackson Labs; Taniguchi *et al.* 2011) mice were genotyped by quantitative PCR (Fig. 1*A–C*; Tesson *et al.* 2002), bred to homozygosity and maintained as homozygous mouse lines. Mouse DNA was extracted from tail snip samples approximately 1–2 mm long using a QIAamp DNA Mini Kit (catalogue no. 51306; Qiagen, Valencia, CA, USA). Multiplex quantitative PCR was performed on extracted mouse DNA using a Stratagene MX3005P Thermocycler (Agilent Technologies, Santa Clara, CA, USA). Sample DNA (1 μl) was added to a qPCR tube (catalogue no. 10011-764; Axygen Scientific, Union City, CA, USA) containing PerfeCTa qPCR Supermix (10 μl, catalogue no. 95063-200; Quanta Biosciences, Gaithersburg, MA, USA), deionized H_2O (7 μl), target primers and a probe with FAM-tagged 5′ and quencher-tagged 3′ ends for the CRE recombinase transgene (1 μl; primer 1: 5′-CCA CCA GCC AGC TAT CAA CTC-3′; primer 2: 5′-CTT AGC GCC GTA AAT CAA TCG-3′; 5′-/56-FAM/CGC CCT GGA AGG GAT TTT TGA AGC/36-TAMSp/-3′; Integrated DNA Technologies, Coralville, IA, USA),

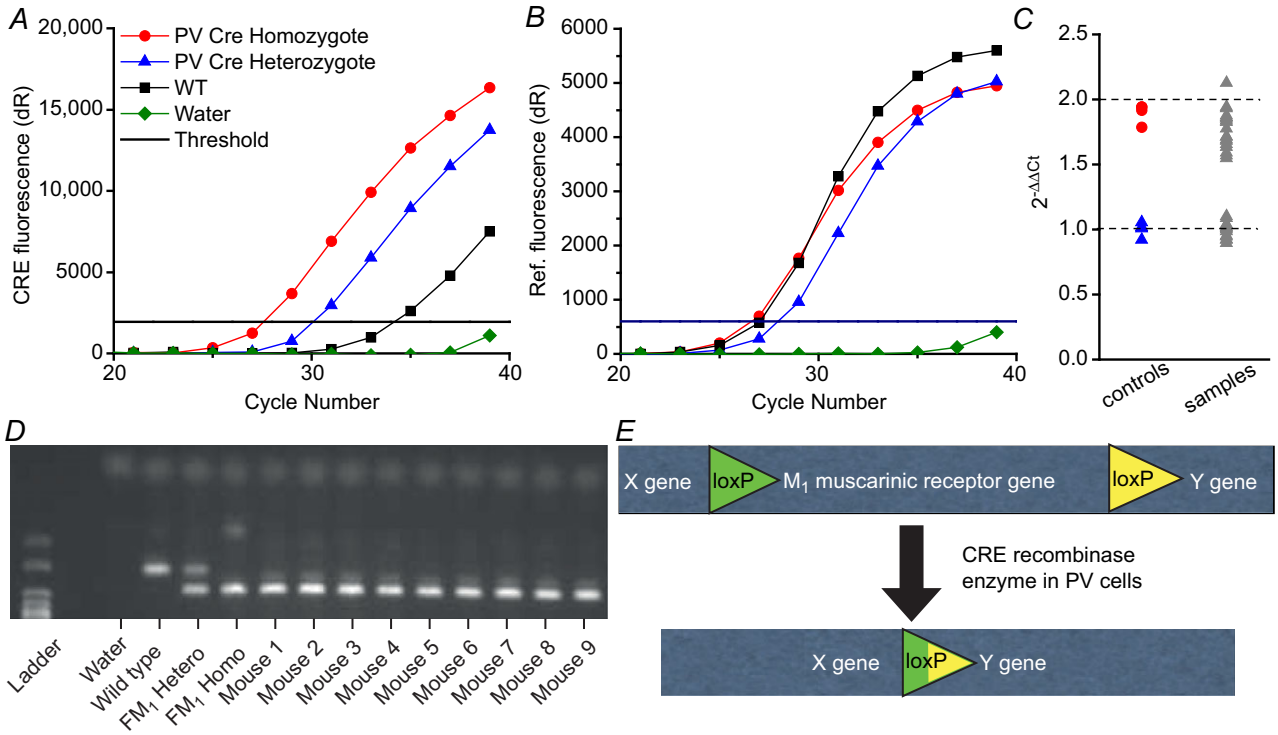

Figure 1. Determination of CRE zygosity and generation of PV-M_1KO mice
A–C, quantitative PCR analyses yield fluorescence *vs.* cycle number plots for (*A*) Fam CRE gene and (*B*) Hex reference gene, enabling the identification of mice containing one (heterozygous), two (homozygous), or no (WT) CRE alleles. *A* and *B*, (red circle) homozygotes, (blue triangle) heterozygotes, (black square) WT and (green diamond) water are indicated. Delta crossing threshold (C_t) is indicated by the black line. (*C*) After normalization to known heterozygous C_ts to 1, unknown samples (grey triangles) separate into C_t that can be categorized as heterozygote or homozygote. *D*, standard PCR illustrating the capacity to distinguish the floxed M_1 transgene band from the WT band. Mice 1–9 were floxed $M_1^{+/+}$. *E*, schematic representation of CRE-mediated deletion of the M_1 mAChR in PV cells, generating PV-M_1KO mice. FM_1, floxed M_1; M_1KO, M_1 mAChR knockout; mAChR, muscarinic acetylcholine receptor; PV, parvalbumin; WT, wild-type.

reference primers and a probe with a HEX-tagged 5′ and quencher-tagged 3′ end for the ultraconserved element uc329 (1 μl; primer 1: 5′-GTC ATC AAG TGA GAA AGA CAT CCT-3′; primer 2: 5′-CAT CAT GAA TTT TGA TAA GCC CAT T-3′; 5′-/5HEX/CTC CTG GCT GCC TGG CTG GC/3IABkFQ/-3′; Integrated DNA Technologies). Following a 10 min hot start at 95°C, DNA was amplified by 40 cycles at 95°C for 30 s and 60°C for 1 min. Using MxPro QPCR Software (Agilent Technologies), fluorescence thresholds were determined via an amplification-based thresholding algorithm with a search range of 5–60%. DNA was determined to be hemizygous or homozygous for CRE by the comparative C_t method. For each reaction, known homozygous ($CRE^{+/+}$, red symbol), known heterozygous ($CRE^{+/-}$, blue symbol), known wild-type (WT; $CRE^{-/-}$, black symbol) and no template control (water, green symbol) samples were used (Fig. 1*A* and *B*). For each unknown sample, $\Delta\Delta C_t$ was calculated by subtracting the ΔC_t of the transgene CRE from the ΔC_t of the reference gene uc329, and normalized based on $\Delta\Delta C_t$ values of known homozygote and heterozygote controls obtained in each run (Fig. 1*C*, grey triangles). To validate results, all samples were run in triplicate and analysed with a pedigree chart. No false zygosity results were observed when samples were assessed via pedigree.

Determination of floxed M_1 and floxed Rosa26YFP mouse zygosity

Mouse blood samples were DNA purified using a Qiagen DNeasy Blood and Tissue Kit (catalogue no. 69506; Qiagen). To determine the presence of the floxed M_1 gene (Kamsler *et al.* 2010), standard PCR was performed on extracted mouse DNA using a C100 thermocycler (BioRad, Hercules, CA, USA; Fig. 1*D*). Sample DNA (50 ng) was added to a master mix containing: 10 × Cl buffer (5 μl), $MgCl_2$ (1 μl), dNTP (1 μl), Taq (0.25 μl), M1C1 primer (2.5 μl; 5′ TCA ACC TGT ACT GGT GAT ACG), M1C2 primer (2.5 μl; 5′ AAC ACT ACT TAC ACG TGG TGC) and M1C3 primer (0.5 μl; 5′ GAG CCT CAG TTT TCT CAT TGG). Five microlitres of ladder was added. The following thermal cycling program was used: 34 cycles of 94°C for 2 min; 94°C for 10 s; 60°C for 45 s; 72°C for 30 s; followed by 72°C for 5 min; and finally 12°C. PCR products were combined with 10 μl of 6× gel loading dye and loaded into wells for gel electrophoresis at 80–120 V for 45–90 min depending on progress. The ultraviolet transilluminator Universal Hood II (Biorad) was used for band determination. In addition, using standard PCR, a homozygous $Rosa26EYFP^{+/+}$ reporter line (stock no. 007920; Jackson Labs; Soriano, 1999; Madisen *et al.* 2009) was generated similarly to that described above. The PCR protocol and set of primer sequences (oIMR9020, oIMR9021, oIMR9102 and oIMR9106) specific to Rosa26YFP mice (stock no. 007920) was obtained from the Jackson Labs web site. All primers used in standard PCR protocols were purchased from Invitrogen (Grand Island, NY, USA).

Generation of PV-Rosa, SOM-Rosa and PV-M_1KO transgenic mice

F_1 heterozygous $PV\text{-}CRE^{+/-}$/$Rosa26EYFP^{+/-}$ mice (referred to throughout the text as PV-Rosa mice) were generated by crossing homozygous PV-CRE and homozygous Rosa26YFP mice. Similarly, F_1 heterozygous $SOM\text{-}CRE^{+/-}$/$Rosa26EYFP^{+/-}$ mice (referred to throughout the text as Som-Rosa mice) were generated by crossing homozygous SOM-CRE and homozygous Rosa26YFP mice. Initially crossing $PV\text{-}CRE^{+/+}$ mice on to the C57BL/6 floxed $M_1{}^{+/+}$ background (Kamsler *et al.* 2010) generated F_1 heterozygous $PV\text{-}CRE^{+/-}$/floxed $M_1{}^{+/-}$ mice, in which M_1 mAChRs are deleted from PV cells (Fig. 1*E*). F_1 mice were then crossed, and the resulting F_2 and F_3 generations were genotyped using PCR and agarose gel electrophoresis to establish separate mouse lines homozygous for floxed $M_1{}^{+/+}$ or floxed $M_1{}^{-/-}$ alleles. For behavioural experiments, floxed $M_1{}^{+/+}$ and floxed $M_1{}^{-/-}$ groups were age matched (7–20 weeks) and contained similar male/female and $PV\text{-}CRE^{+/+}$/$PV\text{-}CRE^{-/-}$ genotype ratios. No significant differences in the performance of behavioural tasks were detected between $PV\text{-}CRE^{+/+}$ and $PV\text{-}CRE^{-/-}$ mice. Thus, $PV\text{-}CRE^{+/+}$ floxed $M_1{}^{-/-}$ and $PV\text{-}CRE^{+/-}$ floxed $M_1{}^{-/-}$ mice were grouped together and are referred to throughout the text as WT mice. $PV\text{-}CRE^{+/+}$ floxed $M_1{}^{+/+}$ and $PV\text{-}CRE^{+/-}$ floxed $M_1{}^{+/+}$ mice were grouped together and are referred to throughout the text as PV-M_1KO mice. Global M_1 KO mice (Hamilton *et al.* 1997) were backcrossed >12 generations on to a C57BL/6 background.

Immunocytochemistry

Mice were transcardially perfused with ice-cold phosphate-buffered saline (PBS) containing (mM): 137 NaCl, 2.7 KCl, 10 Na_2HPO_4, 2 KH_2PO_4, pH 7.4, followed by PBS, 4% paraformaldehyde (PFA, catalogue no.15714-S; Electron Microscopy Sciences Hatfield, PA, USA). Whole brains were postfixed in 4% PFA overnight at 4°C. HC sections (50 μm thick) were then obtained with a Vibratome VT1000 (Leica Microsystems Inc., Buffalo Grove, IL, USA). Slices were either placed in PBS for immediate immunohistochemical experiments or cryopreserved at −20°C in PBS containing 10% sucrose and 50% glycerol. Free-floating sections were washed 3× in PBS and then incubated for 30 min in 0.3% Triton X-100 (catalogue no. BP151–500; Fisher Scientific, Pittsburgh, PA, USA) and 10% donkey serum (catalogue

no. S-30-100ML; Millipore, Billerica, MA, USA) or 7% goat serum (S-1000; Vector Labs, Burlingame, CA, USA) for 1 h, depending on the secondary antibody host. Slices were incubated with the following primary antibodies overnight at 4°C: chicken anti-GFP (directed against YFP, 1:1000, catalogue no. GFP-1020; Aves Labs, Inc., Tigard, OR, USA), mouse anti-PV (1:500, catalogue no. P3088; Sigma-Aldrich, St Louis, MO, USA), rabbit anti-M_1 (1:400, catalogue no. mAChR-M1-Rb-Af340; Frontier Institute Co. Ltd, Hokkaido, Japan) and goat anti-vesicular ACh transporter (1:1000, catalogue no. G448A; Promega, Madison, WI, USA). Slices were then washed three times in PBS and incubated with the following secondary antibodies for 60 min: Alexa Fluor 488 goat antichicken (1:1000, catalogue no. A-11039; Invitrogen), Alexa Fluor 633 goat antimouse (1:1000, catalogue no. A-21050; Invitrogen), or DyLight 649 AffiniPure Donkey Anti-Goat IgG (1:1000, catalogue no. 705-495-147; Jackson ImmunoResearch, West Grove, PA, USA). For anti-M_1 labelling, a goat antirabbit HRP (1:500, catalogue no. NEF812001EA; PerkinElmer Waltham, MA, USA) and a Tyramide Signal Amplification Plus Cyanine Kit (catalogue no. NEL745001KT; PerkinElmer) were utilized, similarly to previously described for *in situ* hybridization (Yamasaki *et al.* 2010). Following secondary staining, slices were incubated with Neurotrace 435/455 (1:100, catalogue no. N21479; Invitrogen) for 20–30 min to label neuronal cell bodies. Specificity of the anti-M_1 antibody to M_1 mAChRs was confirmed using tissue from the global M_1 KO mouse (Hamilton *et al.* 1997). YFP expression in Rosa26YFP mice was intensified using the anti-GFP antibody and Alexa Fluor 488 secondary antibody. Slices were mounted on slides with Vectashield (catalogue no. H-1400; Vector Labs). Images were acquired with a Fluoview confocal imaging system (FV-1000; Olympus America, Center Valley, PA, USA). Primary antibodies were omitted for controls to verify signal and determine noise.

Cell quantification

PV-Rosa mouse tissue was fixed, sliced and stained with anti-GFP and anti-PV antibodies as described above. Fluoview software was used for colocalization between the red and green channels based on thresholding determined by secondary only background controls. The resulting images were saved with anti-GFP (green), anti-PV (red) and co-localized (yellow) channels separated. Images (10×) were stitched together using Fiji's built-in stitching feature to generate an image containing the entire HC. On each stitched HC image, a line was drawn delineating the counting area in CA1 to ensure that the same area was counted between experimenters. Two separate experimenters counted green, red and co-localized cells individually. While counting in Illustrator (Adobe Systems, Inc., San Jose, CA, USA), cells were marked with a symbol to ensure they were not counted twice. Cell counts were averaged and grouped based on laminar distribution in CA1.

Stereotaxic injections of floxed YFP and/or floxed hM3Dq-mCherry AAV into CA1 hippocampus

Floxed YFP (Sohal *et al.* 2009) and floxed hM3Dq-mCherry (Alexander *et al.* 2009; Krashes *et al.* 2011) AAVs ($\sim 10^{12}$ vc ml^{-1}) were obtained from the University of North Carolina Vector Core (Chapel Hill, NC, USA). hM3Dq is a human G_q-coupled M_3 receptor that couples to $G_{q/11}$ proteins and differs from the native human M_3 receptor in two point mutations. These mutations allow the orthosteric ACh binding site to bind clozapine-N-oxide rather than ACh (Armbruster *et al.* 2007). Unless otherwise stated, AAVs were injected into dorsal CA1 HC. WT or homozygous PV-M_1KO mice were anaesthetized with 4% isofluorane, placed ventral side down and secured in the Quintessential Stereotaxic Injector (catalogue no. 53311; Stoelting Co. Wood Dale, IL, USA) apparatus. Artificial Tears Lubricant Ophthalmic Ointment (Akorn Inc., Lake Forest, IL, USA) was gently applied to each eye and the surgery site was cleaned with a povidone iodine preparation solution (catalogue no. 82–255; Aplicare, Meriden, CT, USA). A small mid-sagittal incision was made across the scalp to expose bregma and lambda landmarks. A 33 gauge needle (catalogue no. 7803-05; Hamilton Company, Reno, NV, USA) inserted into a 10 μl syringe (catalogue no. 7635-01; Hamilton Company) was centred on bregma and lateral coordinates of 1.2 mm were used to level the skull in the x direction. Lambda was then located and adjustments were made to level the head in the y direction. The needle was then moved 1.5 mm caudally and 1.4 mm laterally. A small hole was made through the skull using an Ideal Microdrill (catalogue no. 1730; Cellpoint Scientific, Gaithersburg, MD, USA) and the needle was used to puncture the cortex. The needle was then moved 1.1 mm into the brain and 1.5 μl of virus was injected at 0.25 μl min^{-1}. At 1–2 min following viral injection, the needle was slowly removed and the procedure was repeated on the other hemisphere. For ventral CA1, the stereotaxic coordinates were anteroposterior: 2.8 mm, ML: 3.6 mm and DV: 2.3 mm. Following injections, bupivacaine (catalogue no. NDC 0409-1163-01; Hospira, Inc., Lake Forest, IL, USA) was applied topically and the scalp was sutured with nylon suture 5-0 (catalogue no. MV-661; Oasis, Mettawa, IL, USA). Mice that had received stereotaxic injections were monitored postoperatively for 3 days for any signs of pain or distress. Injected mice were used for imaging or electrophysiological recordings approximately 14 days after survival surgery.

Slice preparation

Male and female mice (3–20 weeks for PV-Rosa; 9–37 weeks for AAV injected WT and PV-M_1KO) were used. Electrophysiology experiments utilized PV-M_1KO mice that were confirmed homozygous for CRE through qPCR (see above). PV-Rosa, WT and PV-M_1KO mice were anaesthetized with isoflurane and then decapitated. The brain was placed in ice-cold partial sucrose solution containing (mM): 80 NaCl, 2.5 KCl, 24 $NaHCO_3$, 0.5 $CaCl_2$, 4 $MgCl_2$, 1.25 NaH_2PO_4, 25 glucose, 75 sucrose, 1 ascorbic acid, 3 sodium pyruvate, saturated with 95% O_2/5% CO_2, pH 7.4. Transverse HC or coronal prefrontal cortical slices (300 μm) were cut on a Vibratome 1200S (Leica Microsystems, Bannockburn, IL, USA) and incubated in warm (36°C) oxygenated cutting solution for 30 min before their transfer to a submerged recording chamber (Bischofberger *et al.* 2006). Before each use, the Leica Vibrocheck device was employed to minimize vibration of the blade in the *z*-direction (Geiger *et al.* 2002).

Electrophysiology

Slices were transferred to a submerged chamber and perfused with artificial cerebrospinal fluid (ACSF) solution containing (mM): 125 NaCl, 2.5 KCl, 25 $NaHCO_3$, 2 $CaCl_2$, 1 $MgCl_2$, 1.25 NaH_2PO_4 and 20 glucose, saturated with 95% O_2/5% CO_2, pH 7.4, at 34–35°C. Pyramidal cells or interneurons in CA1 were visualized using IR-Dodt contrast and fluorescence video-microscopy on either a Patch Pro 2000 (Scientifica Ltd, Uckfield, East Sussex, UK) or Infrapatch (Luigs and Neumann, Ratingen, Germany) on an upright Zeiss microscope (Axio Examiner D1; Carl Zeiss Microscopy, LLC, Thornwood, NY, USA). On the Patch Pro 2000, live YFP+ cells were visualized with a blue (470 nm) collimated light-emitting diode (LED) (M470L2-C4; Thorlabs, Newton, NJ, USA) driven by a high-power LED driver with pulse modulation (DC 2100; Thorlabs) or a 505 nm LED (LED4C11-SP; Thorlabs) driven by a four-channel LED driver (DC4100; Thorlabs). On the Infrapatch, a 505 nm LED was controlled by the Colibri LED illumination system (Carl Zeiss Microscopy). Pipettes were fabricated with a 2–4 MΩ tip resistance on a two-step vertical puller (PC-10; Narishige, East Meadow, NY, USA). For loose patch recording, the pipette was filled with extracellular solution, negative suction was applied until a stable access resistance (R_a) of 10–200 MΩ was achieved and action potential (AP) currents (46–1035 pA) were monitored in voltage clamp (holding potential of 0 mV). Loose patch and whole cell recordings were obtained using a Multiclamp 700B amplifier (Molecular Devices, Union City, CA, USA), filtered at 4 kHz and digitized at 20 kHz (Digidata 1440A; Molecular Devices). Solutions were heated to 34–35°C with an inline solution heater (HPT-2, Scientifica; SH-27B/TC-324B, Warner, Hamden, CT, USA). For atropine experiments, slices were pre-equilibrated with 5 μM atropine for at least 30 min before recording. In cases in which PV cells did not exhibit APs in loose patch mode, cells were included in the analysis only if APs could be triggered with an elevated K^+ (7.5 mM) solution. For whole cell recordings, cell-attached seal resistances ranged from 1 to 5 GΩ and R_a ranged from 6 to 20 MΩ. Upon obtaining whole cell mode, 3 min were allowed to stabilize R_a and allow the exchange between cytoplasm and intracellular solution. The intracellular solution contained (in mM): 110 potassium gluconate, 40 KCl, 10 Hepes, 0.1 EGTA, 4 MgATP, 0.3 Na_2GTP, 10 phosphocreatine biocytin 0.2%, titrated to pH 7.2 with KOH, osmolarity 295–305 mosmol l^{-1}. In experiments with GDP-beta-S, Na_2GTP was omitted from the intracellular solution. Bridge balance was used throughout the current clamp experiments and was monitored with a 100 ms long hyperpolarizing current step from –60 mV every 20–60 s, depending on the acquisition protocol. For spontaneous inhibitory postsynaptic current (sIPSC) recordings, a CsCl-based intracellular solution was used (in mM): 123 CsCl, 10 KCl, 30 Hepes, 5 EGTA, 4 MgATP, 0.3 Na_2GTP, 1 QX-314, 10 phosphocreatine and 0.2% biocytin, titrated to pH 7.2 with CsOH, osmolarity 295–305 mosmol l^{-1}. In voltage clamp, access resistance (R_a) was monitored with a −5 mV, 20 ms duration seal test every 30 s. If R_a changed by >20% in either whole cell or loose patch recording modes, the data were excluded from further analysis.

Chemical reagents

DL-APV and QX-314 were obtained from Tocris Bioscience (R&D Systems, Minneapolis, MN, USA). Clozapine N-oxide (CNO) was obtained from Enzo Life Sciences (Pittsburgh, PA, USA). All other chemical reagents were purchased from Sigma-Aldrich.

Data analysis

Acquisition and analysis of electrophysiological data were performed in Axograph X (Axograph Scientific, Sydney, Australia). APs in loose patch and whole cell current clamp were detected by the Event Detection Plug-In Program in Axograph X using the first derivative as a threshold (100–500 pA ms^{-1}). The height of the AP was calculated from the AP threshold to the peak of the first AP during a 100–200 pA depolarizing current from −60 mV. After-deflection (ADF) was defined as the difference between the average voltage in a baseline region 1 ms before the current step and the averaged voltage in a 100 ms time window commencing 200 ms after the termination of the current injection (Cea-del Rio *et al.* 2010). The adaptation coefficient was calculated by dividing the first interspike interval by the last interspike interval of the AP train during

a 700 pA current step. Membrane time constant (τ_m) was obtained by a single exponential fit of the voltage response after a –200 pA current injection from −60 mV in current clamp. Capacitance was calculated by dividing τ_m by the steady-state input resistance (R_{in}). AP half-width was determined from the time to reach 50% of peak to the time to reach 50% during repolarization. Sag ratio (SS/peak) was calculated by dividing the average steady-state voltage response in the last 200 ms by the peak voltage response in the first 200 ms from a 1 s long –150 pA or –200 pA current injection from −60 mV. For event detection of sIPSCs, raw data were digitally filtered at 1 kHz. Optimal detection threshold was determined by calculating the nearest 0.5 increment between two and four times the standard deviation of noise in which the false positive/positive ratio fell below 0.05 (Lawrence *et al.* 2004). sIPSC amplitudes, frequencies and rise times were then measured by the Event Detection Plug-In Program in Axograph X, using a variable template algorithm (0.5 ms 10–90% rise; 10 ms exponential decay, Clements & Bekkers, 1997). To predict the level of depolarization required to reduce the AP amplitude in loose patch mode, the relationship between the first derivative of AP amplitude and depolarization level was determined from a series of depolarizing current steps (+100–700 pA) from −60 mV in current clamp. After being normalized to the maximum rising slope, data from six different recordings were pooled together to obtain a linear regression.

M_1 mAChR signal intensity analysis

Three consecutive confocal slices (0.2 μm steps each) containing a PV cell body and nearby dendrite were *z*-projected to a single flat projection. A rectangular region of interest that contained both the YFP+ cell body or dendrite and adjacent M_1 mAChR labelling within the stratum pyramidale (SP) was defined. The signal intensity of M_1 mAChR (red) and YFP (green) was extracted as a text file using ImageJ. Sequential line series were organized into intensity *vs.* distance traces in Axograph X. Traces (6–20) were averaged and then normalized to the maximum M_1 mAChR intensity (within the neighbouring SP layer) and maximum YFP intensity (within the PV cell). The average M_1 mAChR signal intensity within the YFP PV cell was defined as the cytoplasmic M_1 mAChR signal for soma or dendrites. Channels were acquired sequentially to minimize overlapping excitation of fluorophores.

Anatomical identification of interneurons

Biocytin (0.2%) was included in the recording pipette for *post hoc* morphological identification of recorded cells. After whole cell recording, HC slices were fixed overnight at 4°C in PBS containing 4% PFA, transferred to PBS and kept for up to 2 weeks at 4°C. After permeabilization with 0.3% Triton X-100 in PBS for 2 h at room temperature, slices were incubated in PBS overnight at 16°C with Alexa 633-conjugated streptavidin (final concentration 1 μg ml^{-1}, catalogue no. S-21375; Invitrogen) in PBS. Slices were cryopreserved in PBS containing 30% sucrose and then resectioned at 100–150 μm thickness using a sliding microtome (HM430; Thermo Scientific, Waltham, MA, USA). After staining with Neurotrace 435/455 (1:100 in PBS) and mounting on gelatin-coated slides in Vectashield (catalogue no. H-1400; Vector Labs), sections were imaged with a Fluoview FV-1000 confocal imaging system (Olympus) with a 25× objective (XLPL25XWMP; Olympus, Tokyo, Japan). Confocal stacks (800 × 800 pixels) of interneurons were flat projected, rotated and cropped in PhotoShop 13.0 for display. BCs were defined as having an axonal distribution in the SP (Ribak *et al.* 1978; Buhl *et al.* 1994). Bistratified cells (BiSs) were defined as possessing axon largely restricted to stratum oriens (SO) and stratum radiatum (Buhl *et al.* 1994; Sik *et al.* 1995; Maccaferri *et al.* 2000). Oriens-lacunosum moleculare (O-LM) cells were defined as possessing an axon that projected largely to stratum-lacunosum moleculare (McBain *et al.* 1994; Sik *et al.* 1995). A single cell, consistent with the axon arborizations of an axo-axonic cell (Buhl *et al.* 1994; Freund & Buzsáki, 1996), was observed in which the axon was localized primarily to the border of the SP and SO and possessed collaterals that took on a chandelier-like appearance.

Behavioural screening and testing

Behavioural training was only carried out during daytime hours. Naive mice were used in this study unless otherwise specified. Each mouse underwent a preliminary screen according to standard criteria (Crawley & Paylor, 1997), including home cage behavioural observation, eye twitch, ear twitch, righting reflex and weight. For the righting reflex, the mouse was observed as its cage was gently shaken back and forth to ensure it could maintain balance. The other reflexes were assessed by gently touching the tip of the whiskers, corner of each eye and tip of each ear with a cotton applicator. Mice that failed any of the above criteria were excluded from further testing. One day before each behavioural experiment, mice were individually caged. On the day of testing, each mouse was habituated to the behavioural room environment 30 min before commencement of behavioural testing. Every behavioural experiment utilized an overhead camera and ANY-maze position tracking software (catalogue no. 60005; Stoelting Co.) to record activity. The time of day for each experiment was between 10.00 and 16.00 h and variation in time was equally distributed among test groups. The experimenter was blind to genotype during all behavioural experiments.

After each behavioural experiment, mice were placed back in their original cages or humanely euthanized.

Open field maze

The open field maze (OFM) was adapted from a previously described system (Crawley, 2007). Each mouse was placed in a 40 cm × 40 cm × 35 cm OFM apparatus (catalogue no. 60100; Stoelting Co.) for 60 min. The number of line crossings, rearings, average speed and time immobile were quantified. The same mice used in the OFM were also used in subsequent novel object recognition (NOR) and Morris water maze (MWM) tasks.

Non-rewarded spontaneous alternation T-maze

To assess working memory, mice were subjected to a non-rewarded spontaneous alternation T-maze task (Deacon & Rawlins, 2006), with the addition of a 30 s intra-trial delay to assess the effects of memory load, modelled after Carlén *et al.* (2012). Each arm of the plexiglass T-maze measured 30 cm long, 10 cm wide and 20 cm tall (21st Century Materials, Missoula, MT, USA). The removable plexiglass doors were 10 cm wide, 20 cm tall and approximately 2 cm thick. A permanent floor was omitted so that paper towels lining the bottom could be changed between each mouse. A total of 28 mice were used (PV-M_1KO, $n = 14$; WT, $n = 14$). For each trial, a mouse was placed in the start arm of the maze and allowed to explore until it chose a goal arm. It was then immediately confined to that arm for 15 s using a removable 'door' (thin piece of plexiglass). The door and the mouse were then both removed, and the mouse was placed back into the start area to begin a new choice trial. This was repeated five times. The remaining five trials consisted of the same protocol, except after the mouse was removed from the goal arm it was placed in an empty cage for 30 s before being placed back in to the start arm. After each mouse completed 10 trials, the walls of the maze were wiped down with 30% ethanol and the paper towel flooring was changed.

Novel object recognition

The novel object recognition (NOR) test was performed over the course of 3 days, similar to as previously described (Bevins & Besheer, 2006). The same apparatus (40 cm × 40 cm × 35 cm field) was used as in the OFM. Familiar objects were grey cubes (4.0 cm length); the novel object was a black sphere (4.3 cm diameter; Stoelting Co.). On each day of the test, mice were habituated to the behavioural testing room for 30 min before testing. On day 1, to reduce the novelty effect of environmental exploration, each mouse underwent 20 min of habituation to the OFM. On day 2, two identical grey cube objects were placed in opposite corners of the apparatus and each mouse was allowed 20 min of exploration. On day 3, one of the grey cube objects was replaced with a black spherical object, and each mouse was returned to the field to interact with both familiar and novel objects. Time spent exploring novel and familiar object zones was measured during the first 5 min of testing. The discrimination ratio (DR), calculated as the novel object interaction time divided by the total time interacting with both objects, was statistically compared to the theoretical mean of 0.5 using a parametric one-sample *t* test. Novel object duration on day 3 could not be attributed to a bias in location preference because DR was not significantly different from the theoretical value of 0.5 for both WT and PV-M_1KO mice on day 2 ($P > 0.05$). The experimenter was absent from the room for the duration of the trial. The objects and apparatus were cleaned with 35% ethanol after each trial. An 8 cm perimeter around the object defined the object zone.

Morris water maze

The MWM test was used to evaluate reference learning using spatial cues. The protocol was adapted similarly to that previously described (Vorhees & Williams, 2006). Both groups of PV-M_1KO ($n = 13$) and WT ($n = 12$) mice underwent a 3 day training period and four trials per day (each from a random quadrant) for a total of 12 training trials per mouse. The mice were allowed 45 s to locate a submerged platform placed in a circular tank containing opaque water. Cues were placed around the perimeter of the tank to allow the mouse to use distal cues for navigation to the platform. Mice that did not locate the platform within 45 s were gently guided to it. After 1 day of rest (day 4), the probe trial (1 min long) was conducted on day 5.

Statistical analysis

Statistical analyses were performed with Prism 6 software. Parametric tests were employed, but in cases where population data failed the Shapiro–Wilk normality test, nonparametric tests were employed. For electrophysiological data, two-tailed paired Student's *t* tests or Wilcoxon signed rank test were used for paired tests; Student's *t* tests and Mann–Whitney test were used for two-tailed unpaired tests. The Kolmogorov–Smirnov test was used for the cumulative distribution of data from sIPSC detection. All electrophysiological data are presented as means ± S.E.M. (n = number of recordings) with significance set at $P < 0.05$. For behavioural experiments, data are presented as means ± S.E.M. (n = number of mice); Mann–Whitney test, one-way ANOVA, two-way ANOVA

and Bonferroni's tests were used to evaluate statistical comparisons.

Results

Hippocampal CRE-expressing parvalbumin cells are predominantly comprised of basket and bistratified cells

PV-CRE mice have been used to visualize and manipulate PV cell types in the neocortex and HC (Fuchs *et al.* 2007; Kuhlman & Huang, 2008; Cardin *et al.* 2009; Sohal *et al.* 2009; Murray *et al.* 2011). Although several PV-CRE mouse lines allow the expression or deletion of specific genes from PV cells (Fuchs *et al.* 2007; Chen *et al.* 2010; Wen *et al.* 2010), neither the anatomical identity nor the specificity of CRE-recombinase enzyme expression has been fully established in the HC of these lines.

We crossed homozygous PV-CRE and Rosa26-EYFP reporter mice (Srinivas *et al.* 2001; Madisen *et al.* 2009), creating PV-Rosa mice (see Methods). PV-Rosa mice expressed cytoplasmic EYFP in CRE-expressing cells, enabling PV cells to be visually targeted in acute HC slices (Fig. 2). Twenty-five of 43 YFP+ cells were anatomically identified. Within the CA1 SP (n = 19), we identified PV-Rosa YFP+ interneurons as perisomatically targeting BCs (Fig. 2*A* and *C*; n = 6), dendrite targeting BiSs (Fig. 2*D* and *F*, n = 13) and a single putative axo-axonic cell (n = 1; data not shown). All PV-Rosa interneurons possessed a fast-spiking (FS) phenotype (187.2 ± 12.42 Hz at 700 pA 1 s depolarizing current, n = 30; Fig. 3, Table 1; Zhang & McBain, 1995; Atzori *et al.* 2000; Rudy & McBain, 2001; Lien & Jonas, 2003). PV-Rosa BCs located in CA1

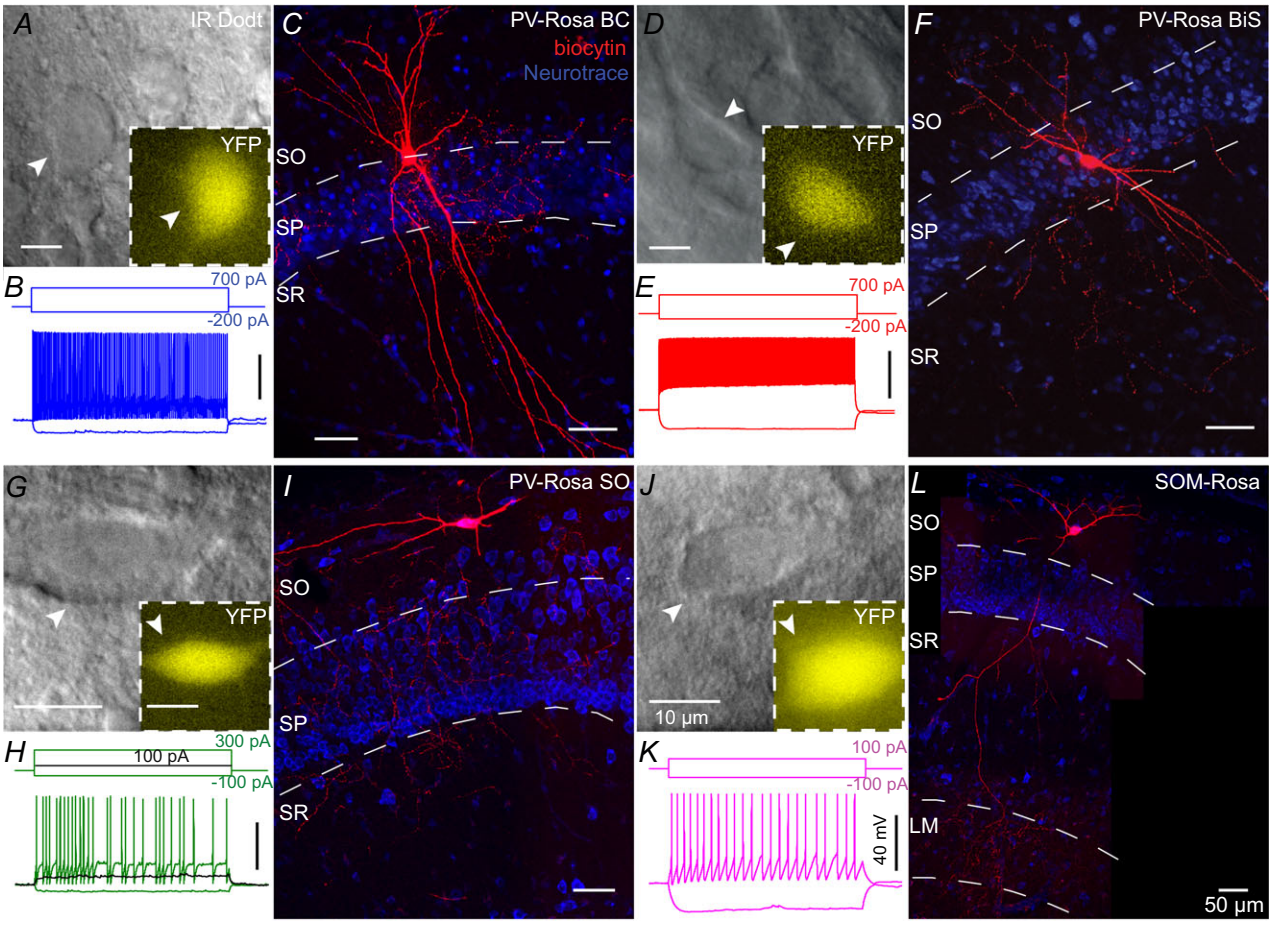

Figure 2. PV-Rosa and Som-Rosa interneurons in the CA1 HC
A, live IR Dodt contrast and 505 nm fluorescent (inset) images of a PV-Rosa interneuron in the hippocampal CA1 SP. *B*, voltage responses to 1 s long hyperpolarizing or depolarizing current steps from the cell shown in *A*. *C*, morphologically identified PV-Rosa BC as revealed by (red) biocytin labelling of the cell in (*A*), counterstained with (blue) Neurotrace 435/455, denoting SO, SP and SR respectively. Fast spiking PV-Rosa BiS interneuron (*D–F*), fast spiking PV-Rosa SO interneuron (*G–I*) and Som-Rosa interneuron (*J–L*) obtained through similar methodology to (*A–C*). Same distance scales: (*A*, *G*, *D* and *J*) and (*C*, *I*, *F* and *L*). Same amplitude and time scales: (*B*, *E*, *H* and *K*). BiS, bistratified cell; LM, lacunosum-moleculare; SO, stratum oriens; SP, stratum pyramidale; SR, stratum radiatum.

SP possessed a prominent apical dendrite and axon that ramified within SP (Maccaferri *et al.* 2000; Bartos *et al.* 2001; Fig. 2*C*). PV-Rosa BCs and PV-Rosa BiSs had similar characteristics in that they were located in SP, exhibited a FS phenotype, were comparable in size, exhibited modest spike frequency adaptation and displayed high sag ratios (Figs 2*A–F* and 3, and Table 1). However, compared to PV-Rosa BCs, PV-Rosa BiSs possessed a significantly higher R_{in} and longer τ_m than PV-Rosa BCs (Table 1). Both vertically and horizontally oriented PV-Rosa SO cells possessed a FS phenotype when depolarized with a large current step (+700 pA; Fig. 3*A*, Table 1), but exhibited a stuttering firing pattern with relatively small current (Fig. 2*H*), which was distinct from PV-Rosa BCs and PV-Rosa BiSs. Morphologically, PV-Rosa SO cells projected mainly to the SP layer, although the axonal arborization occasionally included regions bordering SO and SR (Fig. 2*I*).

O-LM cells in rats have been observed to be weakly PV-positive (Klausberger *et al.* 2003; Klausberger, 2009). To explore the potential overlap between PV-Rosa SO cells and O-LM cells further, we also recorded from SOM-Rosa SO cells (Fig. 2*J–L*). SOM-Rosa SO cells exhibited a significantly lower sag ratio, higher R_{in} and wider half-width than PV-Rosa SO cells (Figs 2*J–L* and 3*B–F* and Table 1), indicating that PV-Rosa SO cells are electrophysiologically distinct from O-LM cells (Fig. 3*L*; Lawrence *et al.* 2006*c*). These parameters are comparable to previous studies indicating that the AP half-width of O-LM cells is wider than that of SO PV-Rosa cells (BCs and BiSs; Fig. 3*C–F* and Table 1; Lien & Jonas, 2003; Gloveli *et al.* 2005; Péterfi *et al.* 2012).

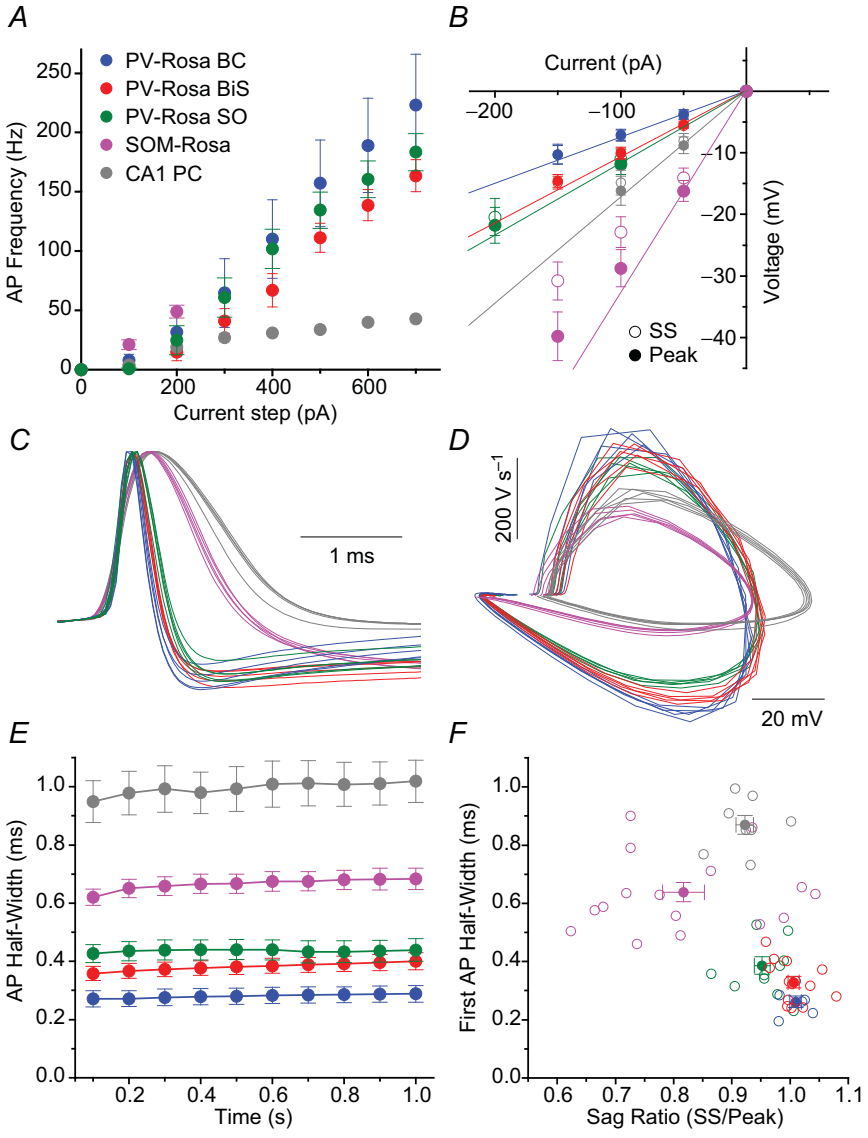

Figure 3. Active and passive properties of PV-Rosa and Som-Rosa interneurons
A and *B*, average AP frequency *vs.* +100–700 pA depolarizing current steps and (*B*) current–voltage relationship for (blue) PV-Rosa BCs ($n = 6$), (red) PV-Rosa BiSs ($n = 13$), (green) PV-Rosa SO interneurons ($n = 11$), (magenta) SOM-Rosa interneurons ($n = 12$) and (grey) a CA1 PC for reference. *B*, open symbols denote SS voltage responses; closed symbols denote peak responses. Continuous lines denote slopes through 0 pA and –50 pA or –100 pA points for peak voltage responses, illustrating a higher sag ratio in PV-Rosa than SOM-Rosa interneurons. *C*, AP waveforms of the first five APs from a representative cell from the respective cell types, showing that PV-Rosa interneuron subtypes exhibit a narrower AP half-width than in the SOM-Rosa interneuron or CA1 PC. *D*, phase plots of dV/dt *vs.* voltage for the respective cell types illustrating a larger dV/dt in PV-Rosa interneurons than the SOM-Rosa SO interneuron or CA1 PC. *E*, population data of AP half-width over the course of a 1 s long, +300–700 pA current step from −60 mV for (blue) PV-Rosa BCs ($n = 6$), (red) PV-Rosa BiSs ($n = 13$), (green) PV-Rosa SOs ($n = 11$), (magenta) Som-Rosa interneurons ($n = 12$) and (grey) CA1 PC ($n = 5$). *F*, scatter plot showing that PV-Rosa interneuron subtypes have a narrower AP half-width and higher sag ratio than SOM Rosa interneurons or CA1 PCs. AP, action potential; BC, basket cell; BiS, bistratified cell; PC, pyramidal cell; SO, stratum oriens; SS, steady state.

Table 1. Intrinsic membrane properties

Property	PV-Rosa BC ($n = 6$)	BP-Rosa BiS ($n = 13$)	PV-Rosa SO cells ($n = 11$)	SOM-Rosa ($n = 15$)	YFP+ WT PV-M_1KO ($n = 8$)	YFP+ Homo PV-M_1KO ($n = 9$)	CA1 PC ($n = 8$)	PV-Rosa PFC ($n = 7$)
R_{in} (MΩ)	66.0 ± 8.7*†‡§¶**††	100.0 ± 7.3¶** 95.6 ± 6.4§¶**††	104.5 ± 5.6¶**	272.9 ± 25.7††	113.8 ± 15.9¶**	139.6 ± 22.2¶**	176.8 ± 23.5**	121.7 ± 13.4
First AP half-width (μs)	261 ± 19†§¶**††	329 ± 20§¶**†† 366 ± 18§¶**††	385 ± 30¶**	639 ± 33††	315 ± 18§¶**††	496 ± 50¶**	870 ± 32††	465 ± 33
First AP height (mV)	45.3 ± 3.8¶	47.8 ± 3.7¶ 51.4 ± 2.4¶	59.0 ± 3.5	52.9 ± 2.0	55.6 ± 2.1¶	55.5 ± 3.4¶	73.4 ± 4.6**††	54.4 ± 2.9
Cm (pF)	115.8 ± 13.3§††	98.8 ± 4.0§†† 98.6 ± 4.1§¶††	88.9 ± 6.0	89.2 ± 7.4	84.6 ± 10.2	76.0 ± 10.0¶	138.7 ± 30.6	75.7 ± 9.4
Sag ratio (SS/peak)	1.0 ± 0.01¶§‡**††	1.0 ± 0.01¶§**†† 1.0 ± 0.0‡§¶**	0.95 ± 0.01**	0.81 ± 0.03††	0.88 ± 0.06	0.77 ± 0.07††	0.92 ± 0.02††	0.97 ± 0.01
τ (ms)	7.1 ± 0.2*†¶**	9.3 ± 0.5¶** 8.8 ± 0.4¶**	9.1 ± 0.9¶**	22.9 ± 1.6††	9.0 ± 1.1¶**	9.9 ± 1.4¶**	21.1 ± 2.5††	8.9 ± 1.0
Adaptation coefficient	0.73 ± 0.10	0.66 ± 0.04¶ 0.7 ± 0.0‡¶	0.77 ± 0.05¶	0.69 ± 0.04††	0.56 ± 0.05††	0.66 ± 0.07	0.47 ± 0.08††	0.80 ± 0.05
Frequency at 700 pA (Hz)	223.3 ± 42.6§	163.6 ± 13.4§ 187.2 ± 12.4§	195.4 ± 18.1§	N.A.	152.9 ± 17.8§	95.4 ± 4.8††	N.A.	184.4 ± 17.2
I_{hold} (pA)	−11.9 ± 42.3	−25.4 ± 10.8¶§ −30.6 ± 13.5¶	−43.8 ± 21.5	−43.0 ± 12.2	−61.0 ± 23.9¶††	−68.9 ± 19.7¶††	66.8 ± 17.3**	29.9 ± 35.1

Values are means ± S.E.M. Abbreviations: AP, action potential; BC, basket cell; BiS, bistratified cell; Homo, homozygous; M_1KO, M_1 muscarinic acetylcholine receptor knockout; PC, pyramidal cell; PFC, prefrontal cortex; PV, parvalbumin; SO, stratum oriens; SS, steady state; WT, wild-type. $^{*}P < 0.05$ compared to PV-Rosa BiSs. $^{\dagger}P < 0.05$ compared to PV-Rosa SO cells. $^{\ddagger}P < 0.05$ compared to YFP+ cells in WT PV-M_1KO mice. $^{\S}P < 0.05$ compared to YFP+ cells in Homo PV-M_1KO mice. $^{\P}P < 0.05$ compared to CA1 PCs. $^{**}P < 0.05$ compared to SOM-Rosa cells. $^{\dagger\dagger}P < 0.05$ compared to PFC PV cells.

To examine the extent and specificity of CRE expression, an anti-PV antibody was used in PV-Rosa mice (Fig. 4*A* and *Ba*). Endogenous YFP (Fig. 4*Bb*) and anti-PV (Fig. 4*Bc*) signals exhibited strong co-localization (Fig. 4*Bd*). Of 281 YFP+ cells, 266 (94.7%) were PV+, while 266 of 333 (79.9%) PV+ cells were YFP+. No statistically significant differences were observed in the number of EYFP+, PV+ and colocalized cells across SO, SP and stratum radiatum layers of HC ($P > 0.05$; Fig. 4*C*), suggesting that CRE was expressed in virtually all PV cells.

mAChR activation enhances PV cell excitability in both CA1 HC and PFC

As cholinergic modulation in both HC and prefrontal cortex (PFC) may be involved in learning and memory (Croxson *et al.* 2011; Hasselmo & Sarter, 2011), we first examined the capacity of mAChR activation to modulate the cellular excitability of PV cells in HC (Cea-del Rio *et al.* 2010) and layer 2/3 PFC (McCormick & Prince, 1985; Erisir *et al.* 1999). Table 1 describes the intrinsic membrane properties of these cells. To isolate the postsynaptic contribution of mAChRs to PV cells, the ionotropic synaptic transmission was blocked with the AMPA receptor antagonist DNQX (25 μM), the NMDA receptor antagonist APV (50 μM) and the $GABA_A$ receptor antagonist gabazine (5 μM). We applied a 1 s long depolarizing current step to PV cells every 20 s while maintaining the recorded YFP+ cells at −60 mV in PV-Rosa mice. In representative recordings from CA1 HC (Fig. 5*A*) and PFC (Fig. 5*D*) YFP+ cells, bath application of 10 μM muscarine enhanced intrinsic excitability in both HC (Fig. 5*B* and *C*) and PFC (Fig. 5*E* and *F*) PV cells. After the offset of the current step, mAChR activation converted the afterhyperpolarization (AHP) to an after-depolarization (ADP) in the HC (Fig. 5*B*, inset) but not PFC (Fig. 5*E*, inset) PV cell. As a population, mAChR activation enhanced AP frequency in both HC (from 80.7 ± 6.6 Hz to 103.5 ± 9.4 Hz, $P = 0.0007$, $n = 8$; Fig. 5*G*, closed circles) and PFC (from 88.5 ± 7.2 Hz to 129.4 ± 12.3 Hz, $P = 0.002$, $n = 7$; Fig. 5*G*, open circles) PV cells. Notably, muscarine application converted the AHP to ADP (from −1.7 ± 0.5 mV to 1.7 ± 1.0 mV, $P = 0.016$, $n = 8$; Fig. 5*H*) and reduced the relative holding current (I_{hold}; from 1.2 ± 1.9 pA to −40.9 ± 10.4 pA, $P = 0.0006$, $n = 8$; Fig. 5*I*) in HC PV cells (open circles). In contrast, the AHP amplitude (from −1.5 ± 0.3 mV to −1.9 ± 0.4 mV, $P = 0.45$, $n = 7$; Fig. 5*H*) and relative I_{hold} (from 0.6 ± 1.0 pA to −16.3 ± 10.0 pA, $P = 0.14$, $n = 7$; Fig. 5*I*) were unchanged in PFC PV cells (closed circles). Therefore, mAChR activation of PV cells exhibited differences in ADF (Fig. 5*H*) and relative I_{hold} (Fig. 5*I*) between HC and PFC PV cells ($P < 0.05$).

These results suggest subtle differences in underlying mechanisms by which mAChRs enhance the excitability of HC and PFC PV cells. Consistent with previous studies (Cea-del Rio *et al.* 2010; Chiang *et al.* 2010), mAChR activation of HC PV cells is accompanied by a prominent ADP (Fig. 5*H*) and change in I_{hold} (Fig. 5*I*). However, these depolarizing features of mAChR modulation were relatively absent from PFC PV cells (Kawaguchi, 1997; Pafundo *et al.* 2013). Although mAChR modulation of both HC and PFC PV cells may contribute to cognitive processes, we focused on HC PV cells in subsequent electrophysiological experiments.

Muscarinic enhancement of action potential frequency in hippocampal CA1 parvalbumin interneurons occurs through direct activation of M_1 muscarinic acetylcholine receptors

To investigate the effect of mAChR activation on PV cell firing frequency under more physiological conditions, we employed non-invasive loose patch recordings from YFP+ cells located in the CA1 pyramidal cell layer of PV-Rosa mice (Fig. 6). In ACSF conditions, 10 of 10 PV cells fired spontaneously (5.7 ± 2.0 Hz). After bath application of 10 μM muscarine, AP frequency was profoundly increased (to 20.9 ± 4.0 Hz; $P = 0.002$, $n = 10$; Fig. 6*A*, *E* and *F*). To examine whether mAChR activation increased PV cell firing through enhanced glutamatergic excitation on to PV cells, we blocked ionotropic glutamatergic transmission with the AMPA and NMDA receptor antagonists DNQX and APV, respectively. Under these conditions, the baseline spontaneous firing frequency was similar to ACSF conditions ($P = 0.24$, Mann–Whitney *U* test, $U(15) = 47$). The muscarine application increased PV cell AP frequency (from 8.8 ± 2.4 Hz in control to 17.2 ± 4.6 Hz in muscarine, $P = 0.033$, $n = 7$; Fig. 6*B*, *E* and *F*) to the same extent as in ACSF conditions ($P = 0.47$). Preincubation with the mAChR antagonist atropine reduced the fraction of PV cells that exhibited spontaneous firing (four of nine were silent) and blocked the mAChR-induced increase in AP frequency (from 5.8 ± 2.7 Hz to 5.6 ± 2.3 Hz, $P = 1.0$, $n = 9$; Fig. 6*C*, *E* and *F*).

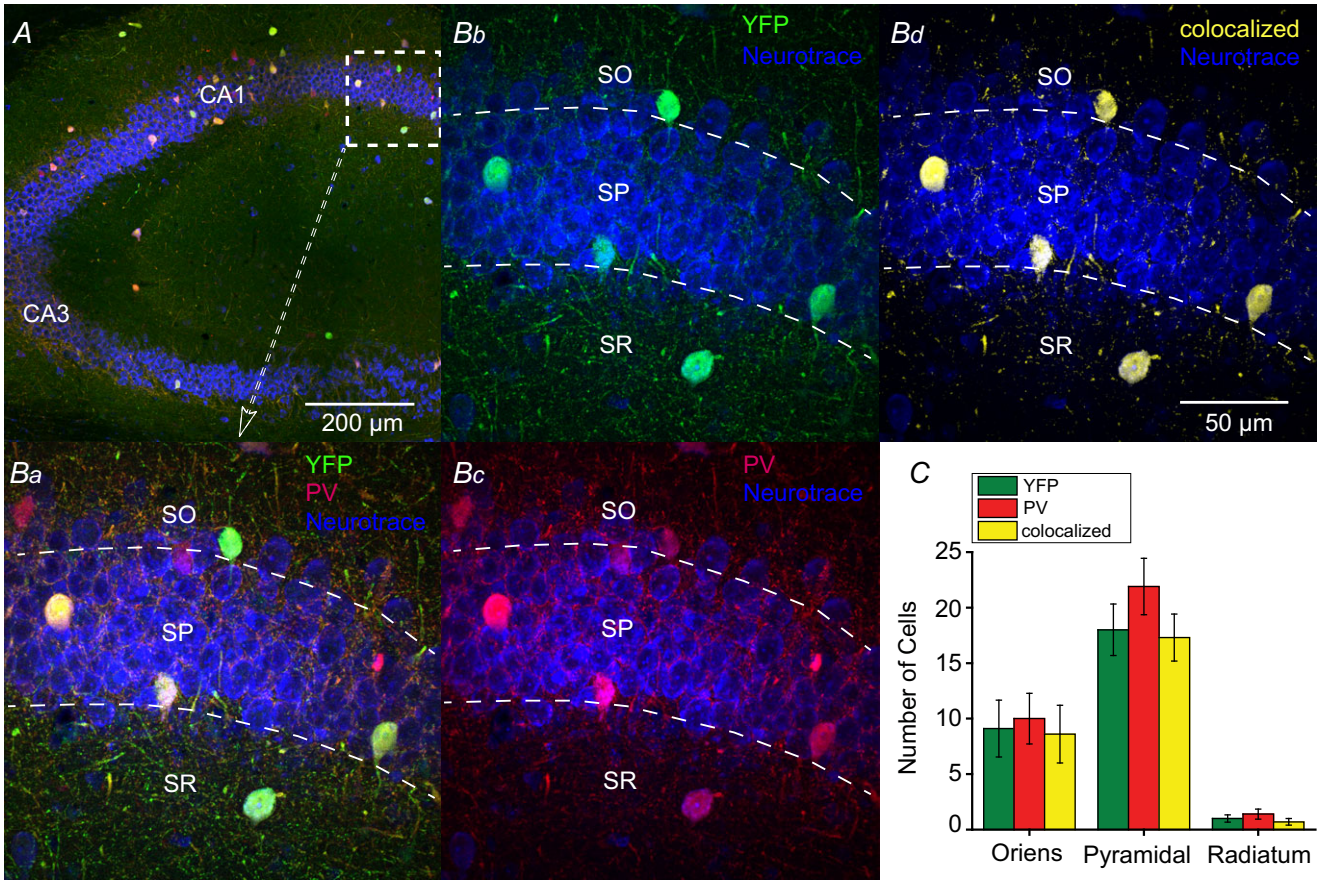

Figure 4. CRE expression in the hippocampus of PV-CRE mice is specific to PV-positive neurons
A, specificity of CRE expression to PV interneurons was confirmed with anti-PV antibody (red) in PV-Rosa mice; YFP+ neurons intensified with an anti-GFP antibody and slices were counterstained with Neurotrace 435/455 (blue). *Ba*, expanded region in (*A*) (dotted box). YFP+ expressing neurons (*Bb*) and PV neurons (*Bb*) in CA1 were overlaid to generate a colocalized channel (*Bd*). *C*, number of YFP+, PV and colocalized neurons were graphed by laminar location. From ten 50 μm thick hippocampal slices ($n = 3$ mice), 18 ± 2.3 EYFP+ cells were located in SP compared to SO (9.1 ± 2.6; Mann–Whitney test, $U_{18} = 18$, $P = 0.0136$, $n = 10$) or SR (1.0 ± 0.33; Mann–Whitney test, $U_{18} = 0$, $P < 0.0001$, $n = 10$). Similarly, the majority of PV cells were located in SP (21.9 ± 2.5) compared to SO (10.0 ± 2.3; Mann–Whitney test, $U_{18} = 15$, $P = 0.0063$, $n = 10$) or SR (1.4 ± 0.45; Mann–Whitney test, $U_{18} = 0$, $P < 0.0001$, $n = 10$). Of 333 cells, no statistically significant differences were observed in the number of EYFP+, PV and colocalized signals across SO, SP and SR layers ($P > 0.05$). PV, parvalbumin; SO, stratum oriens; SP, stratum pyramidale; SR, stratum radiatum.

To examine whether the postsynaptic activation of M_1 mAChRs on PV cells mediated the mAChR-induced increase in PV cell firing, we eliminated M_1 mAChRs specifically from PV cells by generating a mouse line that lacked M_1 mAChRs in PV cells (PV-M_1KO mice; see Methods). Stereotaxic injection of a floxed YFP AAV (Sohal *et al.* 2009) into the CA1 HC of PV-M_1KO mice, which drove expression of YFP in PV cells, enabled us to visualize PV cells in PV-M_1KO mice. Similar to atropine conditions, a comparable fraction of PV cells (three of seven) did not exhibit spontaneous firing in control conditions in PV-M_1KO mice (Fig. 6*Dc*). In addition, mAChR-induced enhancement of AP firing frequency in PV cells was eliminated in PV-M_1KO mice (Fig. 6*D–F*; from 4.6 ± 4.1 Hz to 3.8 ± 3.5 Hz, $n = 7$, $P = 0.25$).

Consistent with a reduction in mAChR-induced depolarization, the mAChR-induced decrease in AP amplitude (ACSF, 83.0 ± 6.5%, $P = 0.034$, $n = 8$, Fig. 7*A*; DNQX+APV, 81.3 ± 2.8%, $P = 0.001$, $n = 6$, Fig. 7*B*), was eliminated in the presence of atropine (106.6 ± 3.5%,

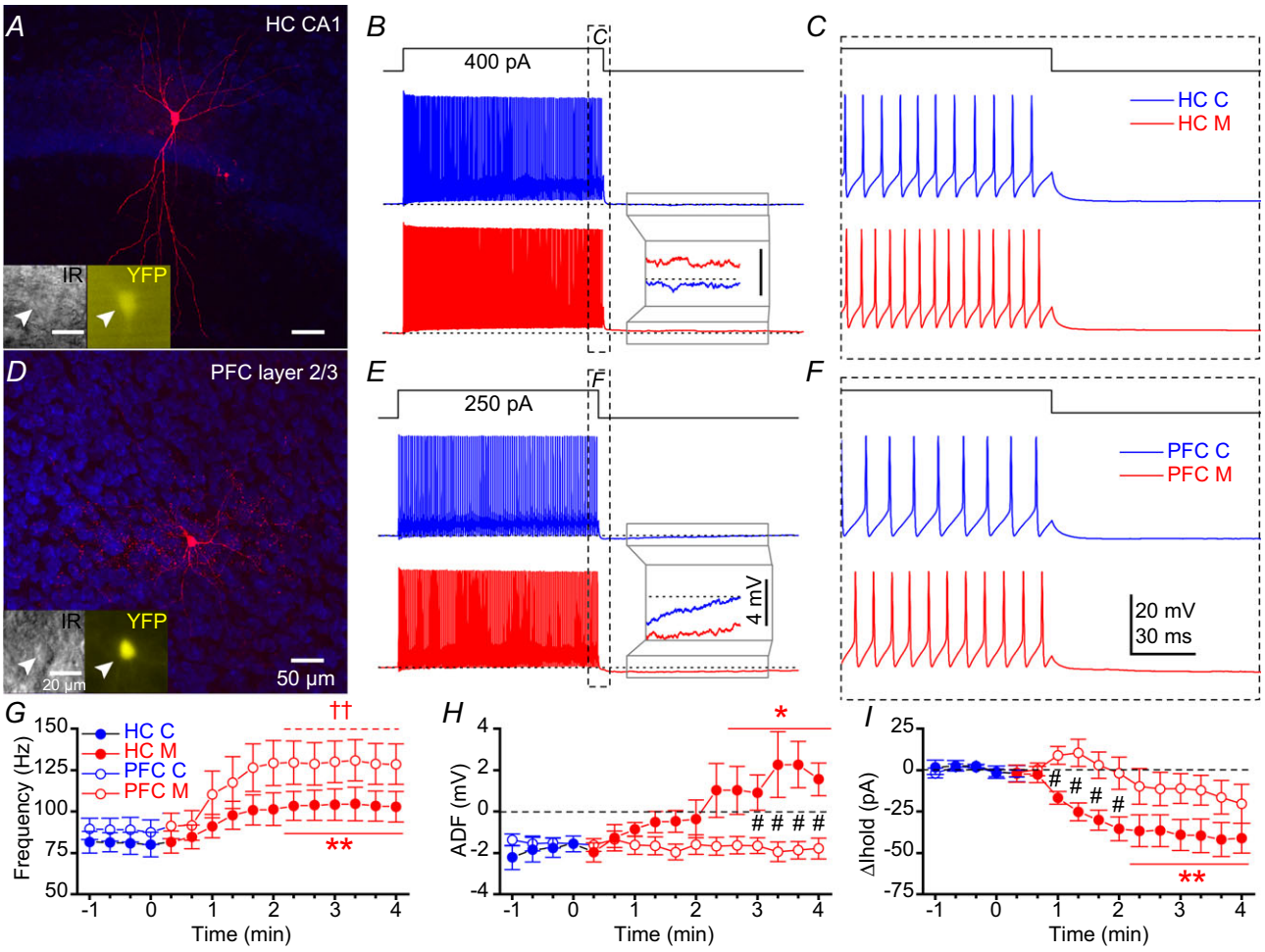

Figure 5. mAChR activation enhances PV-Rosa interneuron excitability in both CA1 HC and PFC
A, biocytin image of a PV-Rosa interneuron in the CA1 HC. Insets, live IR Dodt contrast and YFP (505 nm) fluorescence. *B*, voltage responses upon the introduction of a 1 s long +400 pA current step from –60 mV in a PV-Rosa interneuron in (blue) control and (red) 10 μM muscarine conditions. Inset, expanded region illustrating the conversion of the afterhyperpolarization to an afterdepolarization (dotted line indicates –60 mV baseline). *C*, expanded region in (*B*) displaying mAChR-induced changes in AP firing at the offset of the +400 pA current step. *D–F*, as in (*A–C*), but for a PV-Rosa interneuron in PFC. Note that the afterhyperpolarization is not converted to an afterdepolarization by muscarine. Population data from PV-Rosa cells during wash-in of muscarine summarizing the time course of (*G*) change in AP frequency, (*H*) ADF and (*I*) relative change in I_{hold} from (blue) control to (red; at time 0) muscarine conditions. * and ** denote $P < 0.05$ or $P < 0.01$, respectively, between 3–4 min in muscarine relative to the last min in control (−1 to 0 min) for (closed symbols) HC PV cells ($n = 8$) in *G–I* (paired *t* test for *G* and *H*; Mann–Whitney test for *I*). ††$P < 0.01$ for (open symbols) PFC PV-Rosa cells relative to control (−1 to 0 min) in *G* (paired *t* test). Black # in *H* and *I* denotes $P < 0.05$ between HC PV-Rosa and PFC PV-Rosa cells (unpaired *t* test). ADF, afterdeflection; AP, action potential; HC, hippocampus; mAChR, muscarinic acetylcholine receptor; PFC, prefrontal cortex; PV, parvalbumin.

$P = 0.20$, $n = 3$, Fig. 7*C*) and in PV-M_1KO mice ($103.5 \pm 6.6\%$, $P = 0.63$, $n = 4$; Fig. 7*D*). As AP amplitudes in extracellular recordings are related to the first derivative of intracellularly recorded APs (Henze *et al.* 2000), we determined the relationship between the initial membrane potential and first derivative of APs from 1 s depolarizing current induced AP in whole cell recordings (Fig. 7*E–H*), which probably reflects the availability of functional sodium channels at a given membrane potential. Through linear regression from the reduction in extracellular AP amplitude in loose patch mode ($n = 6$; Fig. 7*I*), mAChR activation was associated with a depolarization in ACSF (4.4 ± 1.7 mV, $P = 0.034$) and DNQX/APV conditions (4.8 ± 0.7 mV, $P = 0.001$) but not atropine (1.7 ± 0.9 mV, $P = 0.20$) or in the PV-M_1KO mouse (0.9 ± 1.7 mV, $P = 0.63$; Fig. 7*J*). Collectively, these data indicate that mAChR-induced modulation of AP frequency occurs through direct activation of M_1 mAChRs on PV cells. Moreover, as indicated by the mAChR-induced reduction in AP amplitude, muscarine depolarized PV cells.

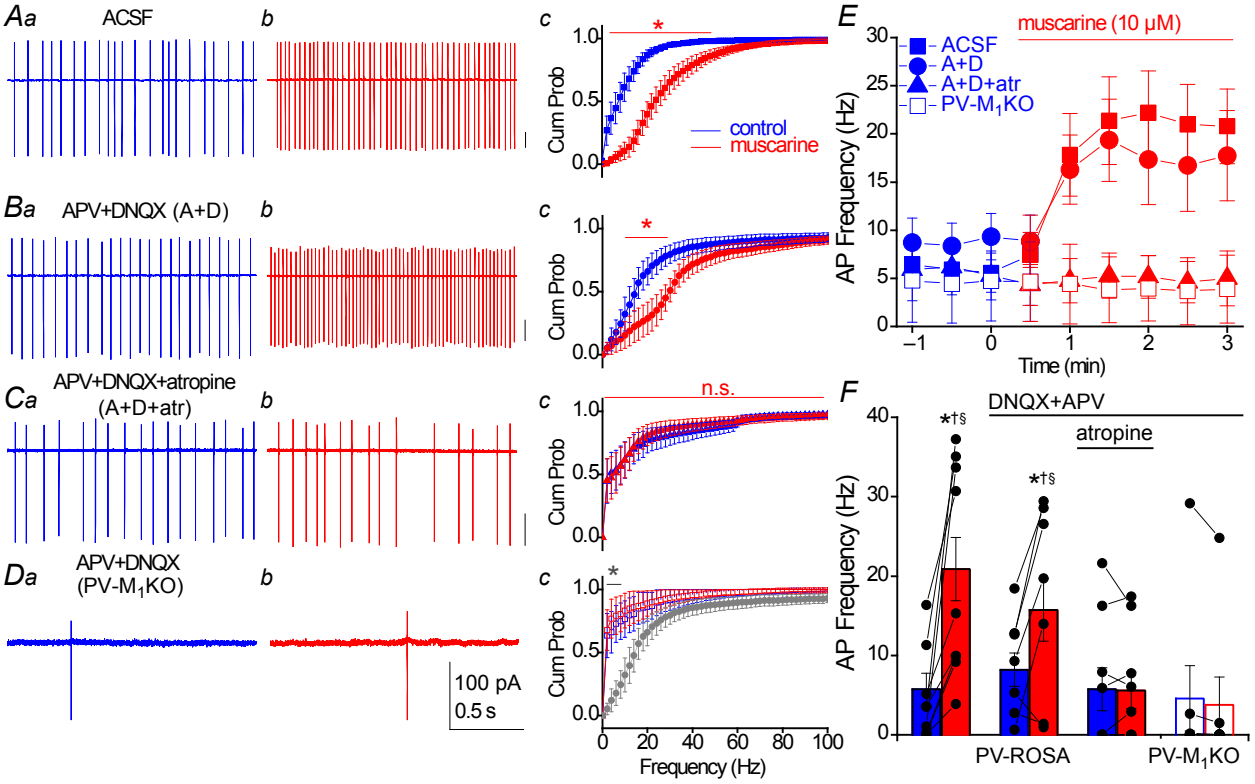

Figure 6. Muscarinic enhancement in AP frequency of hippocampal PV interneurons occurs through direct activation of M_1 mAChRs

A–C, representative recordings obtained under the following conditions: (*A*) ACSF conditions, (*B*) in the presence of ionotropic glutamate receptor antagonists 50 μM APV and 20 μM DNQX or (*C*) in the presence of 50 μM APV, 20 μM DNQX and 5 μM atropine. *A–C*, from PV-Rosa mice. *D*, similar recordings as in (*B*) from a YFP+ neuron in a PV-M_1KO mouse (floxed YFP AAV used to visualize PV cells). For each condition in (*A–D*), representative traces from 2 s long loose patch recordings from PV cells are shown in control conditions (*a*, blue) and after 3 min bath application of 10 μM muscarine (*b*, red). (*c*) Cumulative probability (Cum Prob) distributions of instantaneous AP firing frequencies (2 Hz bin width). A significant difference between (blue) control and (red) muscarine in *Ac* (ACSF: $P < 0.05$ from 2–50 Hz, $n = 10$), *Bc* (DNQX + APV: $P < 0.05$ from 10 to 32 Hz, $n = 7$), but not *Cc* (DNQX + APV + atropine: $P > 0.05$, $n = 9$) or *Dc* (DNQX + APV in PV-M_1KO: $P > 0.05$, $n = 7$; Wilcoxon matched pairs signed rank test). *Dc*, grey asterisk denotes a significant difference ($P < 0.05$ from 2 to 10 Hz) in control conditions between PV-Rosa (grey; same as *Bc*, blue) and PV-M_1KO mice (open symbols, blue; Mann–Whitney test, $n = 7.7$). *E*, time course of change in AP frequency in conditions (*A–D*); muscarine was bath applied at $t = 0$. *F*, summary of the average AP frequency across conditions (*A–D*), comparing the average AP frequency in a 1 min region before muscarine application (blue) and a 1 min region 2–3 min after bath application of muscarine. Asterisks denote $P < 0.05$ for (blue) control *vs.* (red) muscarine conditions (Wilcoxon signed rank test, $W_9 = 55$, $P = 0.002$ for ACSF conditions, $n = 10$; paired *t* test, $t_6 = 2.753$, $P = 0.033$ for DNQX + APV conditions, $n = 7$). In muscarine conditions, AP frequency was also significantly reduced in conditions *C* (DNQX + APV + atropine, †) and *D* (DNQX + APV in PV-M_1KO, §) compared to conditions *A* (ACSF) and *B* (DNQX + APV; Mann–Whitney test, $P < 0.05$). AP, action potential; Cum Prob, cumulative probability; M_1KO, M_1 mAChR knockout; mAChR, muscarinic acetylcholine receptor; PV, parvalbumin.

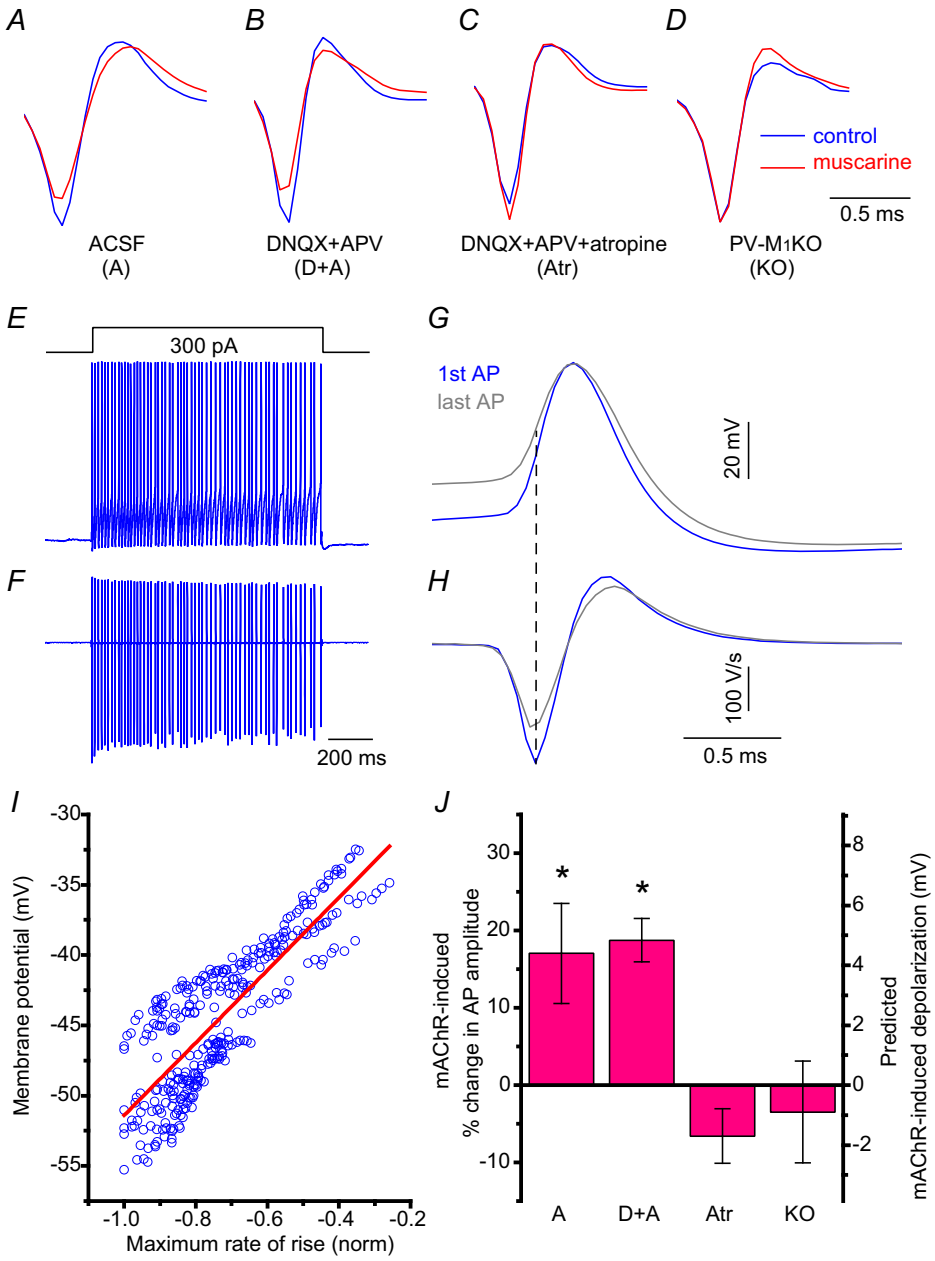

Figure 7. mAChR-induced reduction of AP amplitude
A–C, average AP waveform in loose patch mode in (blue) control and (red) muscarine from APs in Fig. 6*A–C*, respectively corresponding to obtained under the following conditions: (*A*) ACSF conditions, (*B*) in the presence of ionotropic glutamate receptor antagonists 50 μM APV and 20 μM DNQX, or (*C*) in the presence of 50 μM APV, 20 μM DNQX and 5 μM atropine. *A–C*, from PV-Rosa mice. *D*, similar recordings as in (*B*) from a YFP+ neuron in a PV-M_1KO mouse (floxed YFP AAV used to visualize PV cells). Examples of APs obtained in loose patch mode in (*A*) ACSF, (*B*) DNQX and APV, (*C*) DNQX, APV and atropine. *D*, DNQX and APV from a PV-M_1KO mouse. conditions specified in Fig. 6. A train of APs induced in whole cell mode after the introduction of a 1 s long 300 pA current step from −60 mV in a representative PV cell (*E*), time aligned with the first derivative (*F*). *G*,*H*, expanded first (blue) and last (grey) traces in *E* and *F*, showing how maximum rate of rise of the AP relates to the initial membrane potential (dotted line indicate the time point of maximum rate of rise in AP wave in current clamp). *I*, scatterplot of initial membrane potential against maximum rate of AP rise (blue open circles) with linear fit (red) (function: $y = -25.58 + 25.82^{*}x$; correlation coefficient: 0.84; uncorrelated probability. $P = 1e\text{-}87$). *J*, population data showing predicted mAChR-induced depolarization from mAChR-induced percentage change in AP amplitude in the different conditions in *A–D* in loose patch mode (one sample *t* test). AP, action potential; M_1KO, M_1 mAChR knockout; mAChR, muscarinic acetylcholine receptor; PV, parvalbumin.

Genetic deletion of M_1 muscarinic acetylcholine receptors from hippocampal CA1 parvalbumin interneurons diminishes cholinergic excitation of parvalbumin cells

To investigate postsynaptic mechanisms further by which direct mAChR activation enhanced the firing frequency of CA1 PV cells, we employed whole cell patch clamp recordings. As M_1 mAChRs are coupled to G_q, we intracellularly loaded PV cells with GDP-beta-S to test whether postsynaptic disruption of G-protein signalling could block the mAChR-induced enhancement in intrinsic excitability. Using a similar experimental design to that in Fig. 5, we found that PV cells preloaded with GDP-beta-S (15 min) prevented mAChR-induced alterations in intrinsic excitability (from 79.6 ± 12.7 to 65.8 ± 12.6 Hz, $P = 0.12$, $n = 4$), further implicating postsynaptic mAChRs in the cholinergic neuromodulation of CA1 PV cells. In addition, these results indicate that the mAChR-induced increase in PV firing frequency could not be explained by an indirect, network-induced activation of postsynaptic G_q-coupled metabotropic glutamate receptors 1 or 5 (McBain *et al.* 1994; van Hooft *et al.* 2000).

To examine the specific contribution of M_1 mAChRs, we visualized the PV cells with a floxed YFP AAV and obtained whole cell recordings from WT (see Methods) and PV-M_1KO mice (Fig. 8) using an experimental design similar to that used in PV-Rosa mice (Fig. 5). In the presence of DNQX (25 μM), APV (50 μM) and gabazine (5 μM), we applied a 1 s long depolarizing current step to PV cells every 20 s while maintaining the cells at −60 mV in WT or PV-M_1KO mice. In a representative recording from a WT mouse, bath application of 10 μM muscarine increased AP frequency from 69 Hz (Fig. 8*A* and *B*, blue) to 83 Hz (Fig. 8*A* and *B*, red). Moreover, after the offset of the current step, muscarine converted the AHP (Fig. 8*A*, inset, blue) to a small ADP (Fig. 8*A*, inset, red). In contrast, in a PV-M_1KO mouse, mAChR activation did not increase AP frequency (from 63 Hz to 61 Hz) or convert the AHP to an ADP (Fig. 8*C* and *D*, red). As a population, mAChR activation enhanced AP frequency in both WT (from 70.1 ± 6.7 Hz to 97.2 ± 6.2 Hz, $P = 0.008$, $n = 8$) and PV-M_1KO mice (from 77.6 ± 4.7 Hz to 81.9 ± 4.9 Hz, $P = 0.0009$, $n = 9$; Fig. 8*E*), but the mAChR-induced increase in AP frequency was significantly larger in WT than PV-M_1KO mice ($P < 0.001$, Fig. 8*E*). Although mAChR activation reduced the AHP in both WT (from −1.8 ± 0.3 mV to 0.9 ± 1.1 mV, $P = 0.0078$, $n = 8$) and PV-M_1KO mice (from −5.2 ± 0.7 mV to −1.8 ± 1.0 mV, $P = 0.0039$, $n = 9$), only WT mice generated an ADP (Fig. 8*F*). Consistent with that observed in a global M_1 KO mouse (Cea-del Rio *et al.* 2010), the AHP under control conditions was larger in PV-M_1KO mice (−5.2 ± 0.7 mV, $n = 9$) than in WT mice (−1.8 ± 0.3, $n = 9$, $P = 0.0007$; Fig. 8*F*, blue) at comparable AP frequencies ($P = 0.37$). Upon mAChR activation, a larger AHP was also observed in PV-M_1KO mice ($P < 0.05$) than in WT mice (Fig. 8*F*, red). Rin was unaltered during muscarine application (red) in both WT (from 94.4 ± 13.8 to 99.6 ± 16.2 MΩ, $p = 0.25$, $n = 8$; Fig. 8*G*, closed symbols) and PV-M_1 KO mice (from 115.9 ± 15.5 to 118.5 ± 16.7 MΩ, $p = 0.50$, $n = 9$; Fig. 8*G*, open symbols). Activation of M_1 mAChRs depolarized PV cells, as measured by the change in I_{hold}. Although the initial I_{hold} of PV cells in WT and PV-M_1KO mice did not differ under control conditions (−64.9 ± 23.2 pA *vs.* −68.6 ± 20.0 pA, $P = 0.17$), mAChR activation induced a change in I_{hold} in PV cells from WT mice (−91.1 ± 25.8 pA, $P = 0.0078$, $n = 8$) but not in PV cells from PV-M_1KO mice (−10.5 ± 8.4 pA, $P = 0.20$, $n = 9$; Fig. 8*H*). Thus, PV cells from WT and PV-M_1KO mice differed in the capacity to generate mAChR-induced changes in I_{hold} ($P = 0.0016$).

M_1 mAChR activation altered the input–output relationship of PV cells (Fig. 8*I*). M_1 mAChR activation enhanced AP frequency in WT (300–700 pA, $P < 0.05$, $n = 6$; Fig. 8*I*). In contrast, the mAChR-induced increase in AP frequency was eliminated in PV-M_1KO mice (100–700 pA, $P > 0.05$, $n = 7$; Fig. 8*J*, blue *vs.* red) and the dynamic range of AP firing was reduced relative to WT mice ($P < 0.05$ at 600–700 pA; Fig. 8*J*, grey *vs.* blue). The current–voltage relationship, as revealed by −200, −100 and 100 pA current steps from −60 mV (part of the current step protocol displayed in Fig. 8*I* and *J*), also indicated no significant difference ($P > 0.05$) between control and muscarine in both WT and PV-M_1KO mice. No differences in AP threshold (from −35.3 ± 2.5 to −35.9 ± 2.8 mV, $P = 0.20$, $n = 8$) or τ_m (from 10.2 ± 0.7 to 11.0 ± 0.9 ms, $P = 0.31$, $n = 8$) were observed upon mAChR activation in HC PV cells. Finally, differences in mAChR activation between WT and PV-M_1KO mice could not be explained by differences in the subtype of interneuron recorded. Similar proportions of HC BCs, BiSs and SO PV cells were encountered in WT and PV-M_1KO mice and the effects of mAChR activation were similar between these PV interneuron subclasses.

The apparent discrepancy in M_1 mAChR mRNA transcript expression between single cell PCR (Cea-del Rio *et al.* 2010) and *in situ* hybridization (Yamasaki *et al.* 2010) in PV cells led us to compare the protein expression of M_1 mAChRs in PV cells from WT and PV-M_1KO mice. Using a floxed YFP AAV to label PV cells, we examined M_1 mAChR localization in CA1 PV cells from WT and PV-M_1KO mice (Fig. 9). As M_1 mAChRs are trafficked from intracellular pools to the cell surface, we examined intracellular expression of M_1 mAChRs in PV-M_1KO and WT mice in somatodendritic regions, normalizing M_1 mAChR labelling to the surrounding CA1 SP (Fig. 9). M_1 mAChR expression was significantly higher in WT ($n = 6$) than PV-M_1KO ($n = 5$) mice both at somatic (0.25 ± 0.03 *vs.* 0.13 ± 0.02, $P = 0.004$; Fig. 9*G–I*) and

dendritic (0.39 ± 0.08 *vs.* 0.16 ± 0.03, $P = 0.03$; Fig. 9*J–L*) locations. M_1 mAChR expression was also observed in PV cells from CA3, dentate and cortex (data not shown).

mAChR-induced neuromodulation (Fig. 8) and M_1 mAChR expression (Fig. 9) were greatly diminished in PV-M_1KO mice. Despite the selective elimination of M_1 mAChRs from PV cells, we observed no overt deficits in other markers for cholinergic transmission. Cholinergic neuromodulation remained intact in HC principal cells, as indicated by the persistence of M_1 mAChR labelling

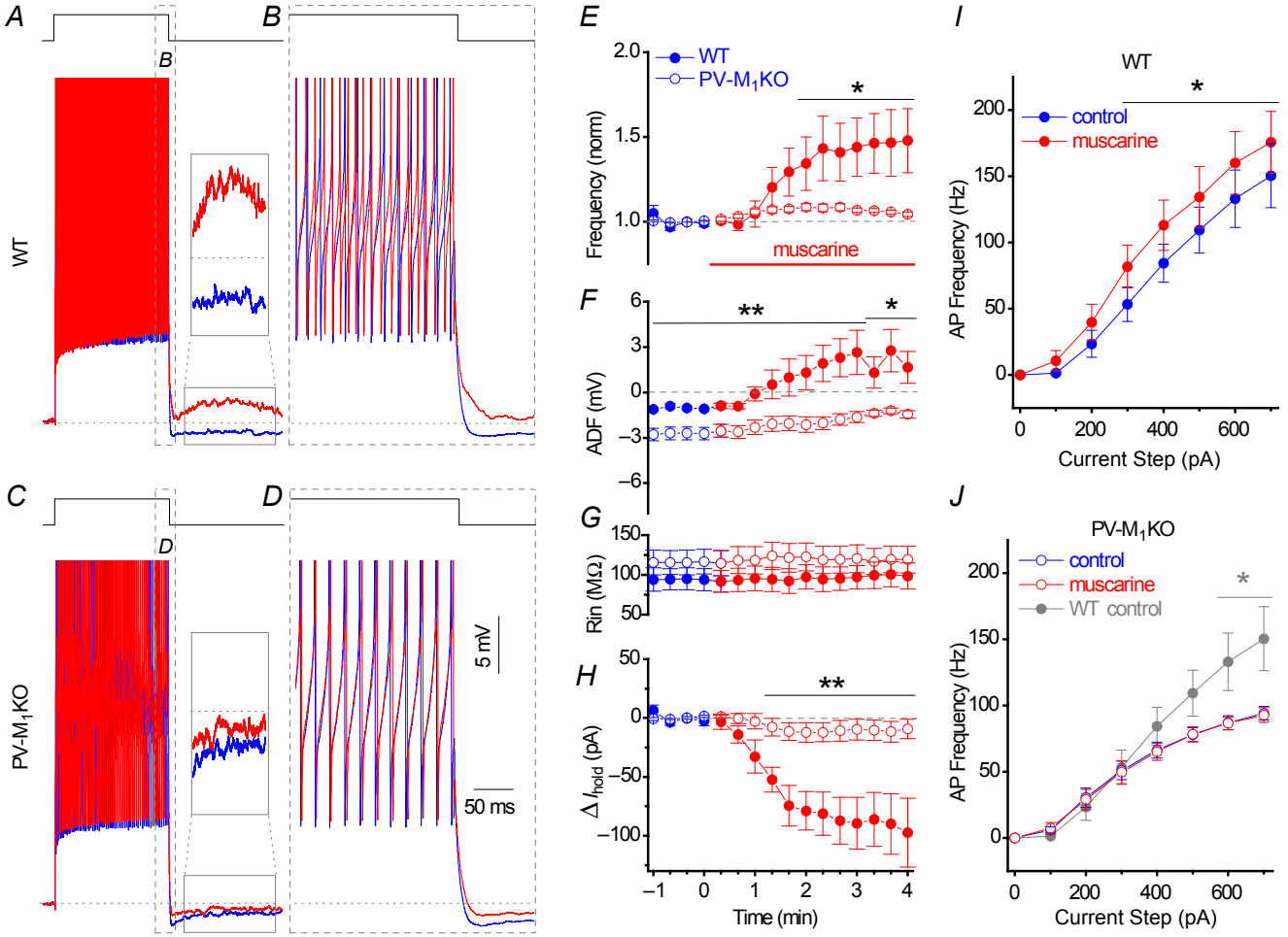

Figure 8. M_1 mAChRs control the cellular excitability of hippocampal CA1 PV cells
A, whole cell voltage responses to the introduction of a 1 s long 500 pA current step from −60 mV in a representative PV cell under (blue) control and (red) 10 μM muscarine conditions (APs truncated for display). Inset, solid box expanded to illustrate the conversion of the afterhyperpolarization to an afterdepolarization (dotted line indicates −60 mV baseline). *B*, expanded region in (*A*) displaying mAChR-induced changes during offset of the 500 pA current step. *C* and *D*, corresponding voltage responses observed in a PV cell from a PV-M_1KO mouse, illustrating that mAChR activation neither increased AP frequency nor converted the afterhyperpolarization to an afterdepolarization. Population data from PV cells summarizing the time course of (*E*) change in AP frequency (normalized to the average AP frequency in a 1 min region before wash-in of muscarine), (*F*) ADF, (*G*) R_{in} and (*H*) relative change in I_{hold} from (blue) control to (red; at time 0) muscarine conditions. * and ** indicate times where significant differences ($P < 0.05$ or $P < 0.01$, respectively) were detected between WT (closed symbols, $n = 8$) and PV-M_1KO mice (open symbols, $n = 9$) in (*E–G*) (Mann–Whitney test). Input–output relationships between AP frequency and current step magnitude (100–700 pA) for WT (*I*; $n = 6$) and PV-M_1KO mice (*J*; open circles, $n = 8$). *$P < 0.05$ for 300–700 pA in WT (paired *t* test, $n = 6$) but not in PV-M_1KO mice (paired *t* test, $P > 0.05$, $n = 8$). Control (blue) and muscarine (red) conditions are indicated. * in *I* denotes $P < 0.05$ between control conditions in (grey) WT and (blue) PV-M_1KO mice (unpaired *t* test, $P < 0.05$ for 600–700 pA). PV cells were visualized with a floxed YFP AAV in both WT and PV-M_1KO mice. ADF, afterdeflection; AP, action potential; M_1KO, M_1 mAChR knockout; mAChR, muscarinic acetylcholine receptor; PV, parvalbumin; WT, wild-type.

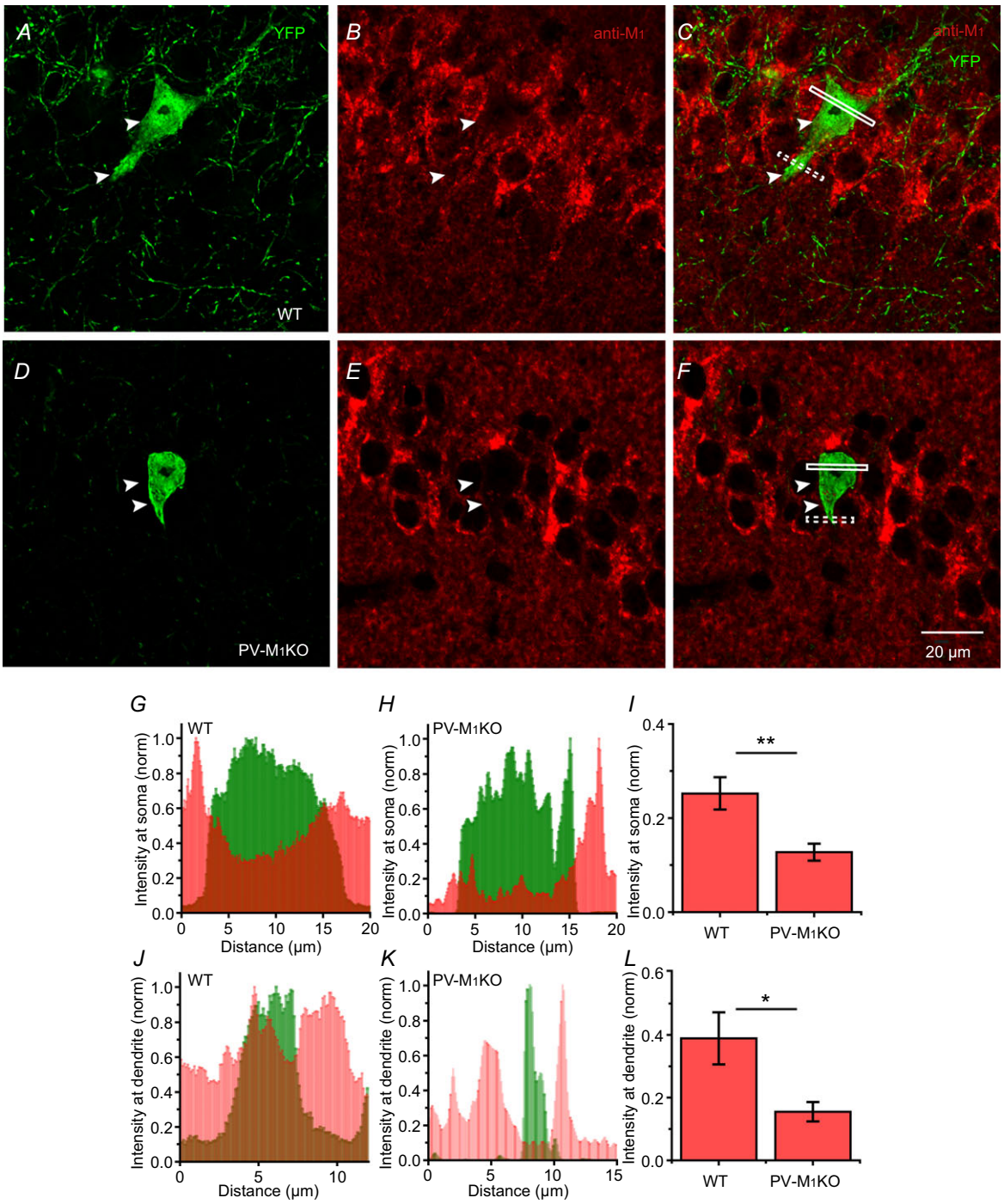

Figure 9. Cytoplasmic M_1 mAChR labelling in hippocampal PV cells at somatic and dendritic compartments from WT *vs.* PV-M_1KO mice
M_1 mAChR intensity (red) was measured in 0.6 μm thick sections through the cell body and dendrite of PV cells (white box for cell body; dotted box for dendrite in *C* and *F*) labelled with floxed YFP AAV (green) in (*A–C*) WT and (*D–F*) PV-M_1KO mice. *G*, somatic M_1 mAChR intensity was measured in the region (white box in *C*) containing cytosolic YFP. M_1 mAChR intensity was normalized relative to the maximum intensity in the neighbouring CA1 stratum pyramidale. *H*, similar analysis as in (*G*) but in a PV-M_1KO mouse. Note the relative absence of M_1 mAChR intensity from the cytosol. *I*, population data showing significant somatic M_1 mAChR intensity of PV cells between WT ($n = 6$) cells and PV-M_1KO ($n = 5$; $P = 0.0043$, Mann–Whitney test, $U_9 = 0$). *J* and *K*, similar analysis as in (*G*) and (*H*) but measured from dendrites of PV cells of WT and PV-M_1KO. *L*, population data showing significant dendritic M_1 mAChR intensity of PV cells between WT ($n = 6$) cells and PV-M_1KO ($n = 5$; $P = 0.03$, Mann–Whitney test, $U_9 = 3$). M_1KO, M_1 mAChR knockout; mAChR, muscarinic acetylcholine receptor; PV, parvalbumin; WT, wild-type.

in the CA1 pyramidal cell layer (Fig. 9*E*), cholinergically induced plateau potentials in CA1 pyramidal cells (Fraser & MacVicar, 1996) and vesicular ACh transporter labelling of cholinergic fibres in the HC (data not shown).

In summary, the combination of electrophysiological and immunocytochemical evidence demonstrates that direct postsynaptic M_1 mAChR activation is a predominant mechanism by which CA1 PV cells undergo muscarinic cholinergic neuromodulation.

Muscarinic activation of parvalbumin cells enhances GABAergic transmission

Cholinergic agonists increase the amplitude and frequency of sIPSCs in CA1 pyramidal neurons (Pitler & Alger, 1992; Behrends & Bruggencate, 1993), raising the possibility that activation of M_1 mAChRs on PV cells (Figs 5, 6 and 8) contributes to the mAChR-induced potentiation of GABAergic transmission. As reported previously that the cholinergic agonist carbachol increases sIPSCs and network oscillations in HC (Pitler & Alger, 1992; Williams & Kauer, 1997; Fisahn *et al.* 1998; Reich *et al.* 2005), we used carbachol (5 μM) to examine mAChR-induced sIPSCs in CA1 pyramidal cells from WT and PV-M_1KO mice (Fig. 10). In the presence of DNQX and APV, in WT (Fig. 10*A*, *C* and *D*, blue; $n = 9$) and PV-M_1KO (Fig. 10*B*–*D*, blue; $n = 8$) mice, baseline sIPSC frequency ($P = 0.54$) and amplitude ($P = 0.16$) were not significantly different. We then examined the capacity of mAChR activation to enhance sIPSCs in WT and PV-M_1KO mice. In WT mice, carbachol increased both IPSC amplitude (from -37.3 ± 3.8 pA to -72.7 ± 11.4 pA, $P = 0.033$, $n = 7$; Fig. 10*A* and *C*) and IPSC frequency (from 12.5 ± 1.1 Hz to 16.8 ± 1.7 Hz, $P = 0.0018$; Fig. 10*A* and *D*). In PV-M_1KO mice, IPSC amplitude (from -33.6 ± 7.2 pA to -56.0 ± 14.1 pA, $P = 0.031$, $n = 6$; Fig. 10*B* and *C*) and frequency (from 9.7 ± 2.4 Hz to 16.4 ± 2.3 Hz, $P = 0.031$;

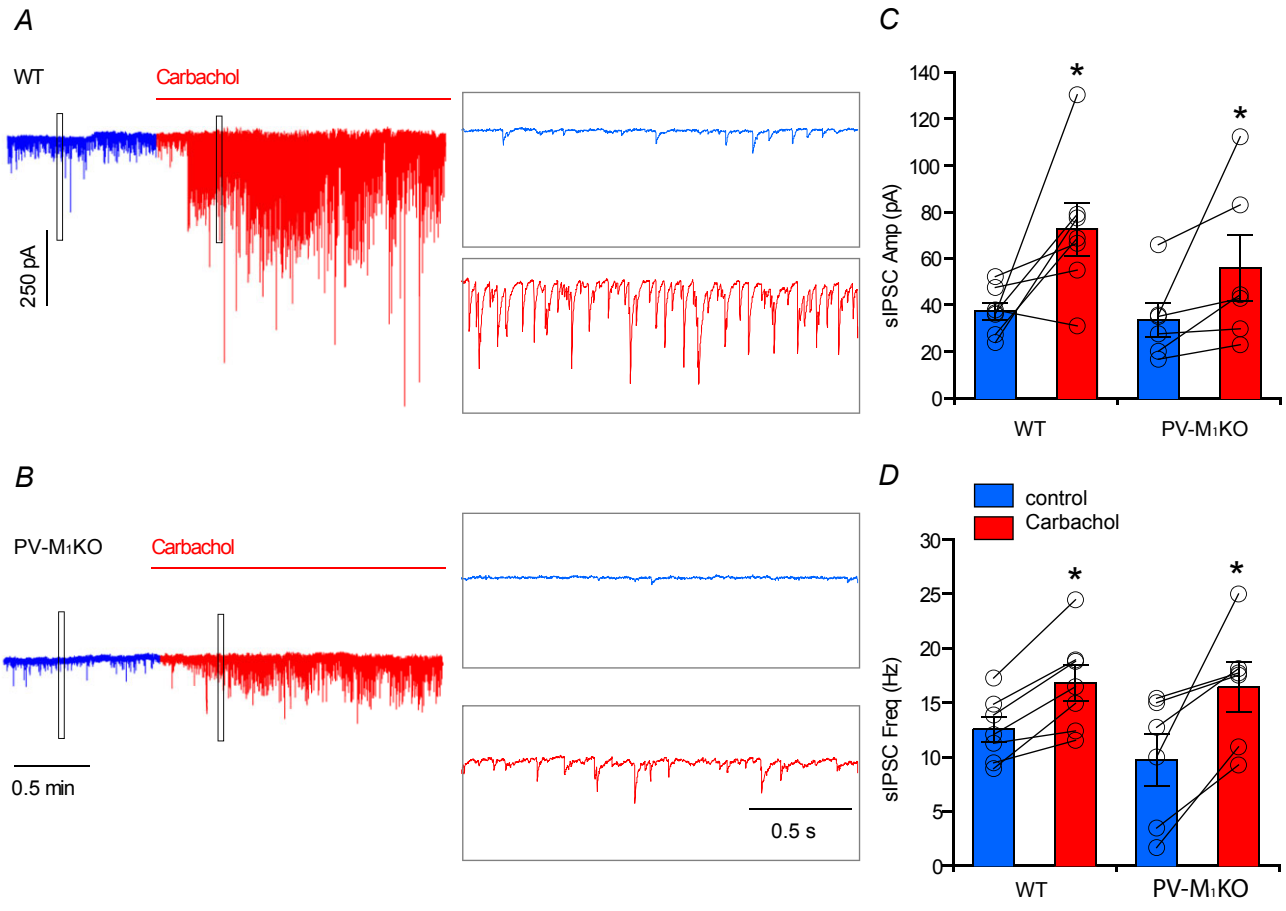

Figure 10. Carbachol evokes sIPSCs from both WT and PV-M_1KO mice
Representative response to carbachol (5 μM) application in (*A*) WT mice and (*B*) PV-M_1KO mice (raw traces displayed). Population data showing the change of sIPSC in (*C*) amplitude and (*D*) frequency in response to carbachol application in WT mice (paired *t* test, $t_6 = 2.75$, $P = 0.0328$; $t_6 = 5.3$, $P = 0.0018$, $n = 7$, respectively), and in PV-M_1KO mice (Wilcoxon matched pairs signed rank test, $W_5 = 21$, $P = 0.0313$; $W_5 = 21$, $P = 0.0313$, $n = 6$, respectively). M_1KO, M_1 muscarinic acetylcholine receptor knockout; PV, parvalbumin; sIPSC, spontaneous inhibitory postsynaptic current; WT, wild-type.

Fig. 10*B* and *D*) were also increased following carbachol application.

The cholinergic enhancement of sIPSCs in CA1 pyramidal cells in PV-M_1KO mice was probably the result of the mAChR-induced activation of non-PV HC interneuron subtypes, such as cannabinoid-sensitive CCK+ interneurons (Reich *et al.* 2005; Cea-del Rio *et al.* 2010, 2012; Nagode *et al.* 2011, 2014) and SOM-positive O-LM cells (Lawrence *et al.* 2006*a*,*c*; Lawrence, 2010). Moreover, mAChR-induced inhibition of GABA release (Pitler & Alger, 1992) from the activation of presynaptic M_2 mAChRs on PV cells (Hájos *et al.* 1998; Hefft *et al.* 2002; Seeger *et al.* 2004; Freund & Katona, 2007; Szabó *et al.* 2010) would be expected to reduce the magnitude and frequency of sIPSCs from PV cells.

To circumvent the confounding influence of mAChRs expressed on non-PV interneuron subtypes, as well as the activation of presynaptic M_2 mAChRs on PV cells, we employed a recently developed technology (Armbruster *et al.* 2007) to activate postsynaptic mAChRs expressed only on PV cells. By expressing an evolved M_3-like mAChR, Designer Receptors Exclusively Activated by Designer Drugs (DREADDs; Alexander *et al.* 2009) in PV neurons (Figs 11*A*–*C* and 12*A*–*F*), we examined the impact of DREADD activation of PV cells on cellular excitability and IPSCs in CA1 pyramidal cells.

Ten days after injection of floxed hM3Dq-mCherry AAV into the CA1 region of PV-CRE mice, we performed whole cell recordings to examine DREADD-induced changes in PV cell excitability. In a representative recorded PV cell (Fig. 11*A* and *B*), hM3Dq-mCherry expression appeared to be restricted to the somatodendritic domain of the biocytin-filled cell, as suggested by the (white) co-localization of (green) hM3Dq-mCherry and (red) biocytin signals (Fig. 11*C*). Activation of hM3Dq with the DREADD-specific agonist CNO (0.5 μM) was similar to mAChR activation with muscarine (Fig. 11*D* and *E*). As a population, hM3Dq activation increased AP frequency (from 80.2 ± 10.7 to 144.7 ± 29.9 Hz, $P = 0.031$, $n = 6$), converted AHP to ADP (from −1.1 ± 0.4 to 1.5 ± 1.0 mV, $P = 0.031$, $n = 6$; Fig. 11*H*) and depolarized PV cells (I_{hold}: from −97.6 ± 19.0 to −188.3 ± 35.0 pA, $P = 0.016$, $n = 7$). There were no significant differences between hM3Dq ($n = 6$) and mAChR ($n = 8$) activation on AP frequency (normalized increase relative to baseline: 1.78 ± 0.23 *vs.* 1.47 ± 0.19, $P = 0.18$; Fig. 11*F* and *G*), ADF (1.5 ± 1.0 *vs.* 1.9 ± 1.1 mV, $P = 0.72$; Fig. 11*H* and *I*), or change in I_{hold} (−90.7 ± 41.0 *vs.* −91.1 ± 25.8, $P = 0.60$; Fig. 11*J* and *K*), respectively.

Having established that CNO excited hM3Dq (Fig. 11) expressed on PV cells (Fig. 12*A*–*F*), sIPSCs were monitored in CA1 pyramidal cells before and after bath application of CNO (Fig. 12*G* and *H*). CNO increased both sIPSC frequency (from 6.9 ± 1.2 Hz to 10.6 ± 1.7 Hz; $P = 0.0008$, $n = 9$; Fig. 12*I* and *K*) and amplitude (from 30.8 ± 5.3 pA to 34.7 ± 6.2 pA, $P = 0.0315$, $n = 9$; Fig. 12*J* and *L*). To investigate the potential origin of IPSCs evoked by DREADD stimulation, we conducted an electrotonic analysis of IPSC waveform by examining the distribution of IPSC rise times in control and CNO conditions. Consistent with an enhancement in GABAergic inhibition originating from electrotonically close somatodendritic locations, CNO increased the frequency of fast rising (0.38–0.42 ms; $P < 0.05$), but not slower rising (0.42–0.90 ms; $P > 0.05$) sIPSCs (Fig. 12*N*). However, there was no significant difference in sIPSC waveform between treatment groups ($P = 0.67$; Fig. 12*M*). Taken together, we conclude that direct muscarinic excitation of PV cells increases the frequency of GABAergic IPSCs.

The role of M_1 muscarinic acetylcholine receptors in parvalbumin cells during locomotor activity and learning

We have established that M_1 mAChRs are expressed on HC PV cells and account almost completely for mAChR-induced alterations in PV excitability. Furthermore, mAChR-induced excitation of PV cells induced IPSCs in CA1 pyramidal cells. Next, using WT and PV-M_1KO mice, we determined the role of M_1 mAChRs on PV cells in a variety of behavioural tasks that have been shown to be sensitive to PV neuronal activity and/or cholinergic neuromodulation.

We first examined locomotor activity. Hyperactivity in global M_1 KO mice (Miyakawa *et al.* 2001; Gerber *et al.* 2001) has been suggested to occur through reduced GABAergic inhibition on to substantia nigral dopamininergic neurons (Gerber *et al.* 2001). As PV cells provide powerful feedforward inhibition to striatal projection neurons (Tepper *et al.* 2010), we examined locomotion of WT (Fig. 13*A*) and PV-M_1KO (Fig. 13*B* and *C*) mice in an OFM. As a population, we found that deletion of M_1 mAChRs from PV cells did not significantly alter locomotor activity, as measured by line crossings (Fig. 13*D*), rearings (Fig. 13*E*), average speed (Fig. 13*F*) and time immobile (Fig. 13*G*; $P > 0.05$). We therefore conclude that M_1 mAChRs on PV cells do not play a major role in normal locomotion.

Next, we examined the role of M_1 mAChRs on PV cells in memory tasks. Global M_1 KO mice exhibit a deficit in working memory but normal spatial memory (Miyakawa *et al.* 2001; Anagnostaras *et al.* 2003). A similar dissociation between these two types of memory occurs with the disruption of PV cell function (Murray *et al.* 2011; Carlén *et al.* 2012). NMDA receptor ablation in PV cells also impairs object recognition memory (Korotkova *et al.* 2010). Therefore, we investigated the performance of WT and PV-M_1KO mice in several learning paradigms. In a T-maze spontaneous alternation task, which is a test

of working memory, there was no significant difference in alternation rates between PV-M_1KO mice and WT mice ($F_{(1,52)} = 0.99$; $P = 0.32$; Fig. 14*A* and *B*). However, there was a significant interaction in time ($F_{(1,52)} = 10.24$; $P = 0.0023$). A Tukey's *post hoc* multiple comparisons test revealed that 1 s and 30 s intratrial periods were different within PV-M_1KO ($P = 0.04$) but not within WT mice ($P = 0.29$), suggestive that PV-M_1KO mice exhibited a mild delay-dependent working memory deficit. Therefore, our results are consistent with the involvement of M_1 mAChR activation of PV cells in normal working memory.

In the NOR task, a two-way ANOVA on WT and PV-M_1KO groups indicated a significant interaction in object time ($P = 0.0018$). WT mice spent more time with

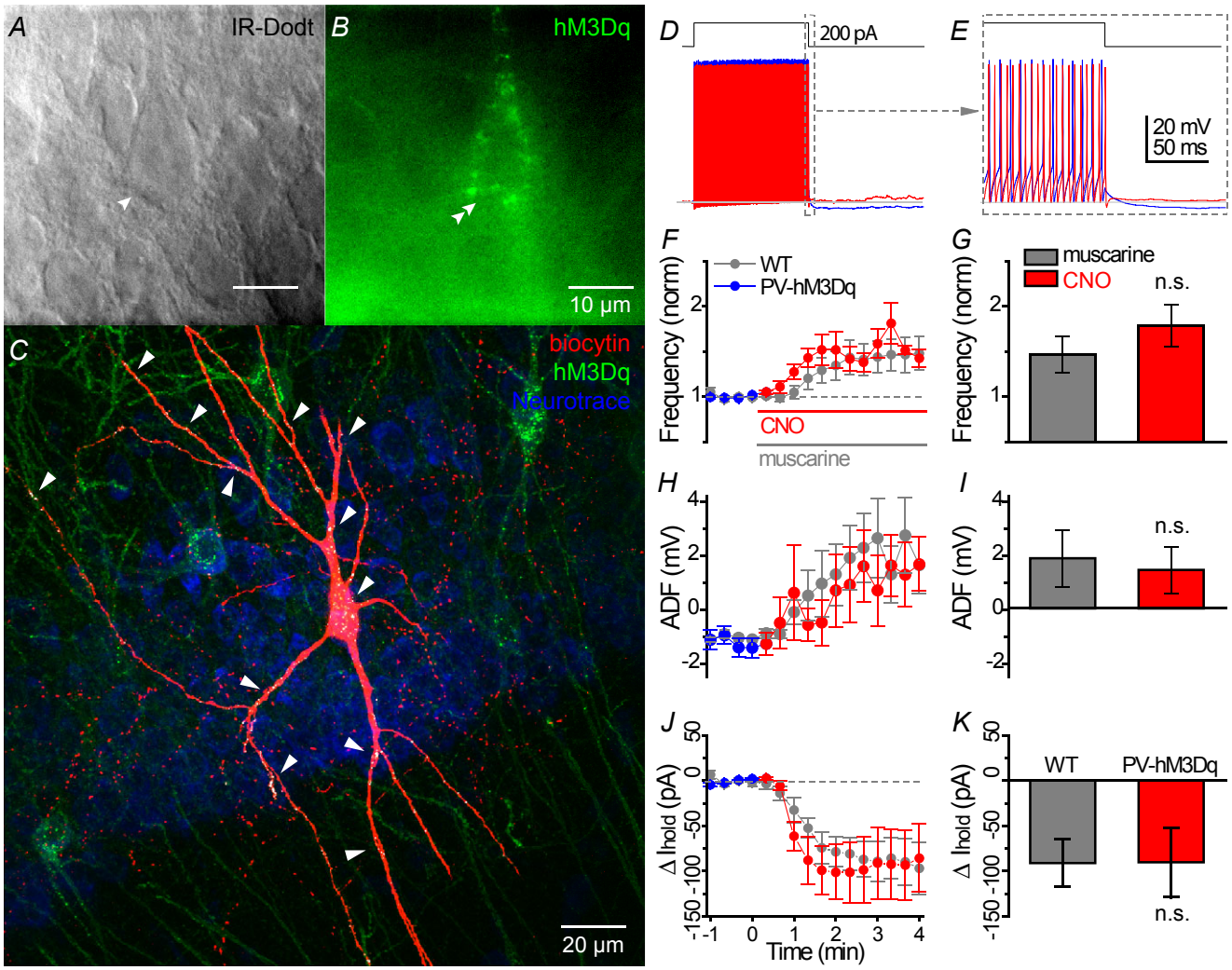

Figure 11. hM3Dq-induced changes in the cellular excitability of hippocampal CA1 PV cells
A and *B*, live IR Dodt contrast and 590 nm fluorescent image of a hM3Dq-mCherry expressing PV cell in the hippocampal CA1 stratum pyramidale. The mCherry signal was pseudocoloured green to distinguish between the 633 nm biocytin signal in (*C*). *C*, morphologically identified PV basket cell as revealed by (red) biocytin labelling of the cell in (*A*), with white labelling indicated by white arrows showing hM3Dq-mCherry in somatodendritic regions only. *D*, whole cell voltage responses to the introduction of a 1 s long +200 pA current step from −60 mV in a representative PV cell under (blue) control and (red) 500 nM CNO conditions. *E*, expanded region in (*D*) displaying muscarinic acetylcholine receptor-induced changes in afterhyperpolarization during offset of the 200 pA current step. Population data from hM3Dq-expressing PV cells summarizing the time course of (*F*) change in action potential frequency (normalized to the average action potential frequency in a 1 min region before wash-in of muscarine), (*H*) ADF, (*J*) relative change in I_{hold} from (blue) control to (red; at time 0) CNO conditions. *Times where significant differences ($P < 0.05$) were detected between muscarine activation of PV cell WT (grey, $n = 8$) and CNO activation of hM3Dq-mCherry expressing PV cells in PV-CRE mice (coloured, $n = 7$) in (*E*–*G*) (multiple *t* test). *G*, *I* and *K*, bar graph showing no significant difference between muscarine-induced and CNO-induced effects on intrinsic excitability, ADF and I_{hold} (Mann–Whitney test). ADF, afterdeflection; CNO, clozapine N-oxide; PV, parvalbumin; WT, wild-type.

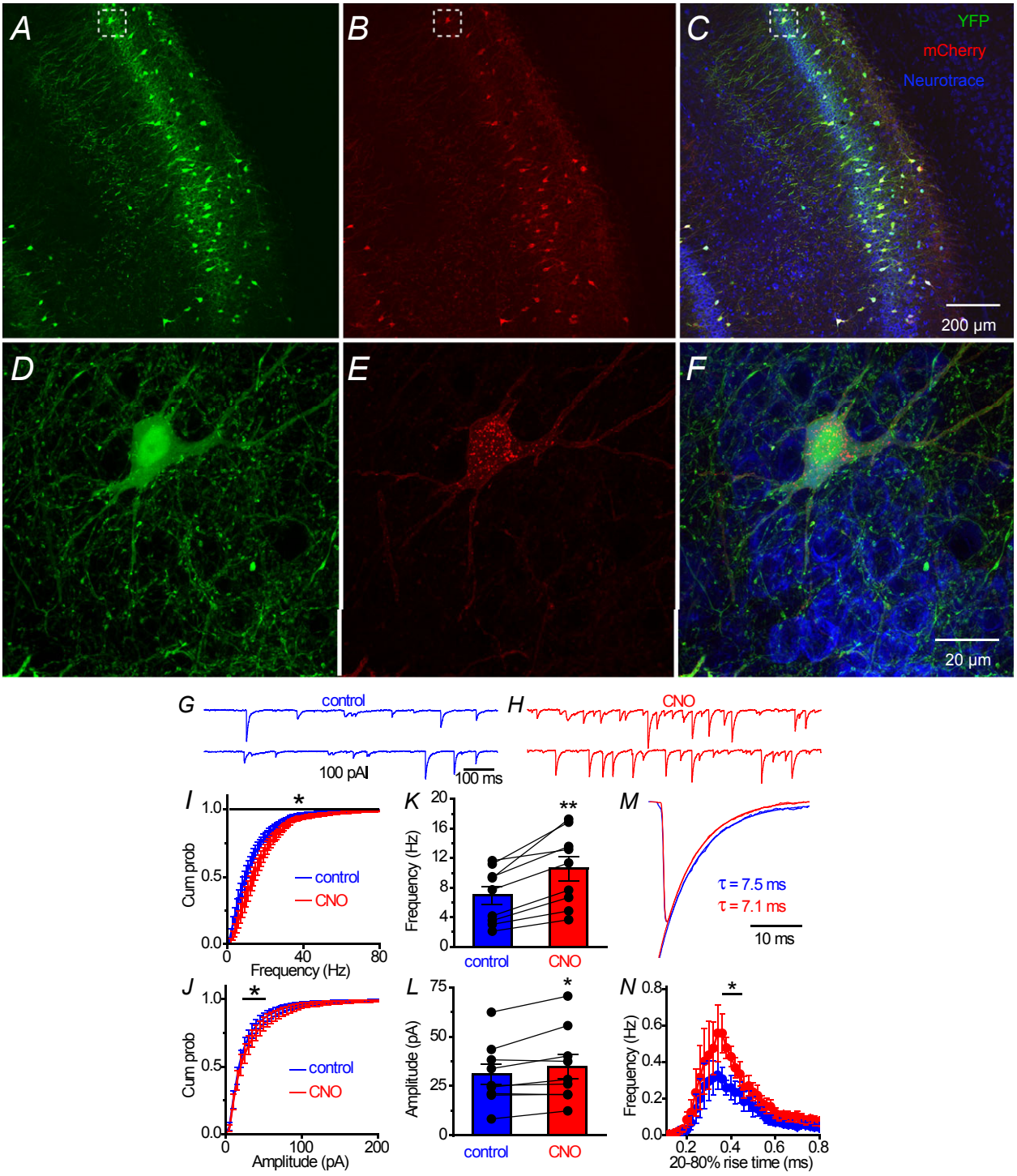

Figure 12. hM3Dq activation of PV cells enhances GABAergic transmission in CA1 pyramidal cells
Floxed YFP and floxed hM3Dq-mCherry AAVs were stereotaxically injected simultaneously into ventral CA1 of PV-CRE mice. Images are of (*A*) cytosolic YFP, (*B*) hM3Dq-mCherry or (*C*) both channels merged. *D–F*, expanded areas from dashed white boxes in (*A–C*). Representative 1 s traces of sIPSCs in (*G*) control conditions and (*H*) after bath application of DREADD agonist CNO. Cumulative probability for frequency (*I*) and amplitude (*J*) of sIPSC. Population graphs for sIPSC (*K*) frequency (paired *t* test; $t_8 = 5.2$, $P = 0.0008$, $n = 9$) and (*L*) amplitude ($t_8 = 2.6$, $P = 0.032$, $n = 9$) under (blue) control or (red) CNO conditions. *M*, averaged sIPSC waveform in control and CNO. *N*, event histogram of 20–80% rise time of sIPSCs in a 2 min window (blue) 2 min before and (red) 4 min after CNO application. sIPSCs with rise time of 0.38–0.42 ms were enhanced by CNO (multiple *t* test, $P < 0.05$ $n = 9$). CNO, clozapine N-oxide; PV, parvalbumin; sIPSC, spontaneous inhibitory postsynaptic current.

the novel (14.4 ± 2.4 s) than familiar object (6.8 ± 1.5 s, $P = 0.0173$; Fig. 14*C* and *E*). In contrast, time spent with novel (14.6 ± 3.2 s) and familiar objects (9.2 ± 2.1 s) was not significantly different in PV-M_1KO mice ($P = 0.093$, $n = 13$; Fig. 14*D* and *E*). Consistent with these results, WT (0.69 ± 0.04, $P = 0.0011$, $n = 12$) but not PV-M_1KO (0.56 ± 0.07, $P = 0.43$, $n = 13$) mice exhibited a DR that was significantly above the theoretical mean of 0.5. Therefore, our results reveal that M_1 mAChRs on PV cells are important in recognition memory.

Finally, we assessed spatial reference memory in the MWM (Vorhees & Williams, 2006). Both WT ($n = 12$; Fig. 14*F*, *G* and *J*) and PV-M_1KO mice ($n = 13$; Fig. 14*H–J*) exhibited a significant reduction in latency to locate the platform on day 3 compared to day 1 ($P < 0.05$; Fig. 14*J*), indicating that spatial learning was intact. Furthermore, the two groups did not differ in latencies to locate the platform within each day of training ($P > 0.05$; Fig. 14*J*) or during the probe trial ($P = 0.60$, $U_{23} = 68$; Mann–Whitney test).

Taken together, consistent with findings in global M_1 KO mice (Miyakawa *et al.* 2001; Anagnostaras *et al.* 2003), and mice in which PV function has been disrupted (Murray *et al.* 2011), our results suggest that M_1 mAChRs on PV cells are important for working and recognition memory but not reference memory.

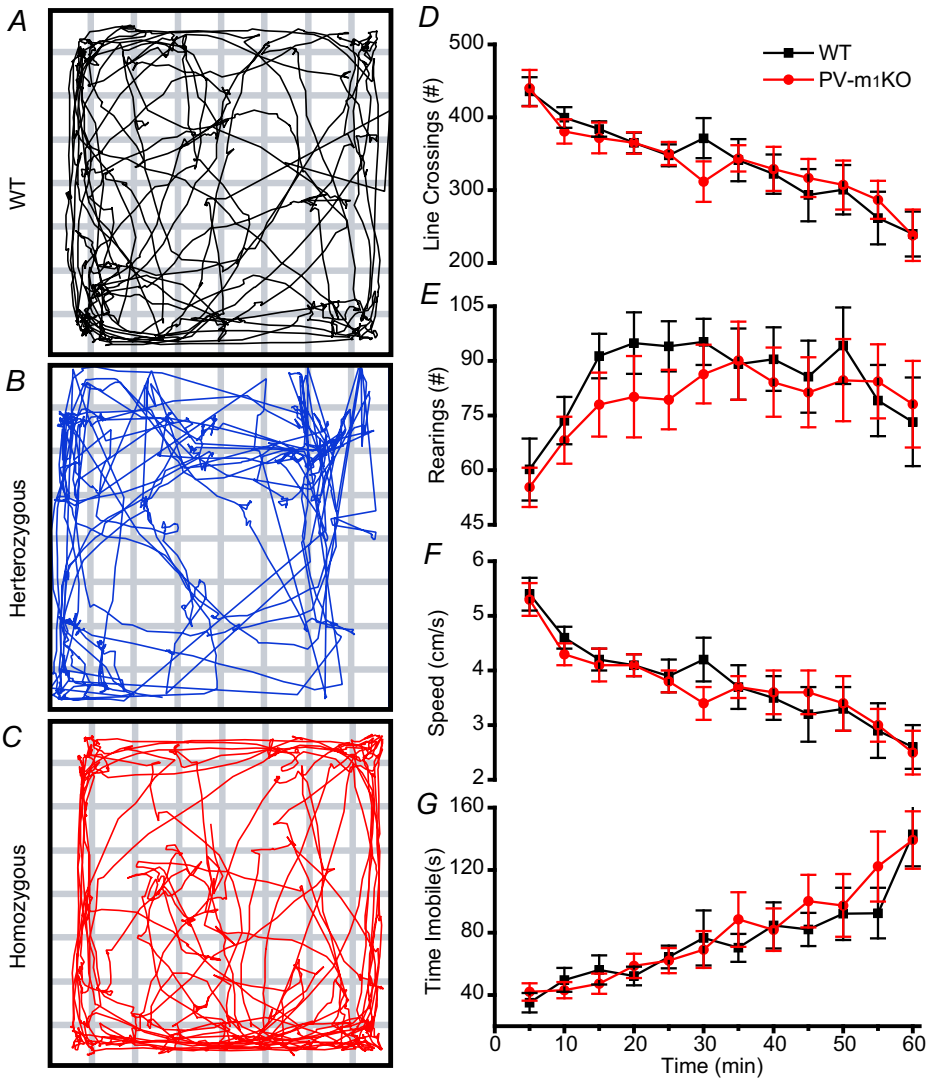

Figure 13. PV-M_1KO mice exhibit no locomotor deficits in the open field maze
Representative track plots of a (*A*) WT, (*B*) heterozygous and (*C*) PV-M_1KO mouse during the first 5 min in the open field maze. (*D*) line crossings, (*E*) rearings, (*F*) speed and (*G*) time immobile over the course of 60 min, binned in 5 min averages ± S.E.M. for (black rectangles) WT ($n = 12$) and (red circles) homozygous PV-M_1KO ($n = 13$) mice. No significant difference between mouse lines was observed at any of the time intervals ($P > 0.05$, Mann–Whitney test). M_1KO, M_1 muscarinic acetylcholine receptor knockout; PV, parvalbumin; WT, wild-type.

Discussion

In the present study, we eliminated M_1 mAChRs from PV interneurons using transgenic technology and gained insights into the role of M_1 mAChRs on PV cells in the regulation of cellular excitability *in vitro* and *in vivo*.

Cholinergic modulation of parvalbumin interneuron subtypes through M_1 muscarinic acetylcholine receptors

Unlike previous studies that utilize PV-CRE mice to investigate PV circuit function and behaviour (Fuchs *et al.* 2007; Sohal *et al.* 2009; Chen *et al.* 2010; Murray *et al.* 2011), we anatomically identified specific PV interneuron subtypes that expressed CRE recombinase. Using PV-Rosa mice, we found that CRE-expressing cells in CA1 were comprised mainly of PV BCs and PV BiSs (Fig. 2), consistent with known PV interneuron subtypes (Freund & Buzsáki, 1996; Klausberger & Somogyi, 2008). FS PV interneurons are often associated with perisomatic inhibition, attributable to the enrichment of PV cells in SP. However, by expressing EYFP at a high level in PV cells, we discovered that BiSs were also a prevalent PV cell type in CA1 SP. Therefore, in addition to PV BCs that provide perisomatic inhibition, PV BiSs probably play a major role in HC PV circuitry and corresponding modulation of HC function (Tukker *et al.* 2007). Despite this under-reported abundance of PV BiSs, IPSCs evoked from PV cells rise rapidly (20–80% rise time <0.5 ms, Fig. 12), suggesting that IPSCs originating from BiSs and BCs

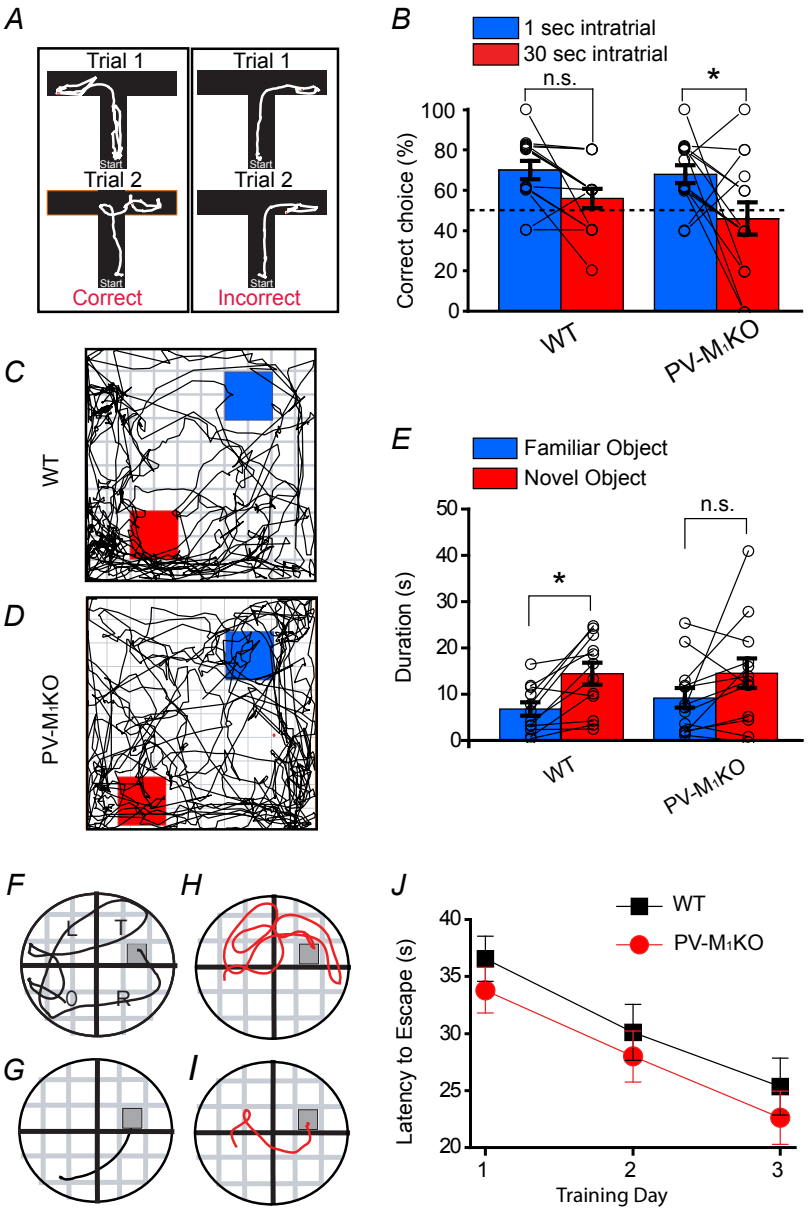

Figure 14. Performance of PV-M_1KO mice in T-maze, novel object recognition and Morris water maze tasks
A, examples of correct and incorrect choices in the spontaneous alternation T-maze. *B*, in a T-maze spontaneous alternation task there was no significant difference in alternation rates between PV-M_1KO mice and WT mice ($F_{(1,52)} = 0.99$; $P = 0.32$). However, there was a significant interaction in time ($F_{(1,52)} = 10.24$; $P = 0.0023$). Representative track plots of a (*C*) WT mouse and (*D*) PV-M_1KO mouse during the 5 min test novel object recognition task. *E*, as a population, WT ($n = 12$) but not PV-M_1KO ($n = 13$) mice spent significantly more time with the novel than familiar object (object time: $F_{(1,23)} = 12.44$, $P = 0.0018$, two-way ANOVA, Bonferroni multiple comparisons test). Representative track plots are shown for a WT mouse on (*F*) training day 1 and (*G*) training day 3 in Morris water maze; (*H*) and (*I*) are corresponding plots for a PV-M_1KO mouse. *J*, population data indicate that both WT ($P < 0.05$, $n = 12$) and PV-M_1KO ($P > 0.05$, $n = 13$) mice exhibited a significant reduction in latency to escape between days 1 and 3 (time effect: $F_{(2,69)} = 6.64$, $P = 0.0023$, two-way ANOVA, Bonferroni multiple comparisons test). No significant differences were found on days 1–3 between WT and PV-M_1KO mice (genotype effect: $F_{(1,69)} = 1.15$, $P = 0.29$, two-way ANOVA, Bonferroni multiple comparisons test). M_1KO, M_1 muscarinic acetylcholine receptor knockout; PV, parvalbumin; WT, wild-type.

undergo a similar degree of dendritic filtering (Maccaferri *et al.* 2000). Therefore, loss of M_1 mAChRs from BiSs and BCs (and to a lesser extent axo-axonic cells) may contribute to the behavioural differences observed in PV-M_1KO mice.

The activation of M_1 mAChRs on HC PV cells increases firing frequency (Figs 6 and 8), increases holding current at −60 mV and transforms the AHP to an ADP (Fig. 8). A similar increase in excitability is observed in PFC HC cells but does not feature a prominent depolarizing component (Fig. 5). In PV-M_1KO mice, excitatory effects of muscarine (Figs 6 and 8) and M_1 mAChR expression (Fig. 9) are almost eliminated in HC PV cells. Under control conditions, HC PV cells from PV-M_1KO mice exhibited a larger AHP (Fig. 8*F*) than in WT mice, similar to PV BCs from global M_1 KO mice (Cea-del Rio *et al.* 2010). PV cells from PV-M_1KO mice also exhibited a reduced number of PV cells that fired spontaneously (Fig. 6*Dc*) and altered the dynamic AP frequency range (Fig. 8*J*). As PV cells express Kv7.2 and Kv7.3 channels (Cooper *et al.* 2001; Geiger *et al.* 2006), M_1 mAChR activation probably inhibits a Kv7/KCNQ/M current (Lawrence *et al.* 2006*b*, *c*; but see Rouse *et al.* 2000). Also consistent with that observed in global M_1 KO mice (Cea-del Rio *et al.* 2010), M_1 mAChR activation induced an inward current in PV cells from WT but not PV-M_1KO mice (Fig. 8*H*). Therefore, M_1 mAChR modulation of PV BC and BiS cells probably involves the inhibition of Kv7/KCNQ/M and AHP conductances and the activation of a cationic conductance (Lawrence *et al.* 2006*c*). It is possible that M-current inhibition is offset by a cationic conductance to yield no net change in cellular conductance (Fig. 8*G*). Interestingly, the activation of M_3 mAChRs (hM3Dq-mCherry) in PV cells induced similar functional responses to that observed with endogenous M_1 mAChRs (Fig. 11), suggesting that M_1 and hM3Dq receptors must be similar enough in localization and probably couple to the same effectors. In contrast, in CCK BCs, M_3 and M_1 mAChRs are not interchangeable because the elimination of M_1 or M_3 mAChRs are associated distinct mAChR-induced effects on excitability (Cea-del Rio *et al.* 2010).

M_1 mAChRs are also expressed on PV cells in cortical regions (Disney & Aoki, 2008) and undergo muscarinic modulation (Pafundo *et al.* 2013 but see Kawaguchi, 1997). Although mAChR modulation of the intrinsic excitability of PV cells appears to be a common cellular mechanism, our study is in accordance with previous studies that HC PV cells exhibit a more prominent mAChR-mediated ADP (Cea-del Rio *et al.* 2010) and postsynaptic depolarization (Cea-del Rio *et al.* 2010; Chiang *et al.* 2010; Szabó *et al.* 2010) than cortical PV cells (Kawaguchi, 1997; Gulledge *et al.* 2007; Pafundo *et al.* 2013). Such differences in the level of direct mAChR-induced depolarizing drive suggest that HC PV cells are less reliant on glutamatergic synaptic drive than PFC PV cells to become engaged during network oscillations (Pafundo *et al.* 2013). Finally, similarly to CCK BCs (Cea-del Rio *et al.* 2010) and CCK Schaffer collateral-associated cells (Widmer *et al.* 2006; Cea-del Rio *et al.* 2011; Bell *et al.* 2013), a mild mAChR-induced hyperpolarizing holding current preceded depolarization in PFC PV BCs (Fig. 5*I*). However, I_{hold} was not significantly different than control conditions. Moreover, in contrast to CCK interneurons (Cea-del Rio *et al.* 2010, 2011), AHPs of PFC PV BCs were resistant to mAChR-induced modulation (Fig. 5*H*). Therefore, PV interneurons may exhibit some overlapping features of mAChR-induced modulation, but the specific underlying mechanisms vary on a subtype-specific basis, limiting the extent that mAChR-induced modulation of PV cells can be generalized.

Do synaptically activated M_1 muscarinic acetylcholine receptors on parvalbumin interneurons contribute to network dynamics?

Though many interneuron subtypes participate in cholinergically dependent oscillations (Buzsáki, 2002), the mechanisms by which ACh modulates the synchrony of specific HC and PFC circuits remain poorly understood. PV interneurons participate in theta oscillations (Klausberger & Somogyi, 2008) and are thought to be essential for the generation of gamma rhythms (Bartos *et al.* 2007; Buzsáki & Wang, 2012). HC PV BCs receive four to five times higher glutamatergic input than principal cells (Gulyás *et al.* 1999; Glickfeld & Scanziani, 2006), providing a mechanism for generating gamma activity through glutamatergic excitation of PV interneurons (pyramidal cell-interneuron gamma or PING; Bartos *et al.* 2007; Fuchs *et al.* 2007). Evidence for a PING mechanism exists, for example, in the CA3 HC, where perisomatically generated IPSCs play a key role in the generation and maintenance of cholinergically induced oscillations (Atallah & Scanziani, 2009; Oren *et al.* 2010). However, carbachol increases the frequency of spontaneous inhibitory events in the absence of glutamatergic transmission, implying that HC interneurons are also directly excited by mAChR activation (Pitler & Alger, 1992; Behrends & Bruggencate, 1993). Optogenetic approaches can also excite PV interneurons directly to generate interneuron gamma (Cardin *et al.* 2009; Sohal *et al.* 2009), providing a mechanism by which the direct modulation of PV excitability *in vitro* and *in vivo* can contribute to the generation of neuronal rhythms. In this study, we find that mAChR activation of HC CA1 PV cells produces an increase in AP frequency regardless of whether glutamatergic excitation is intact, and that the mAChR-induced increase in AP frequency is eliminated in M_1 mAChR-lacking PV cells (Fig. 6*D*). This observation suggests that direct M_1-mediated depolarization of PV cells can enhance inhibitory synaptic transmission and enhance oscillatory power through the recruitment of PV cells. Consistent

with the capacity of HC networks to be influenced through the muscarinic depolarization of PV cells, DREADD-induced stimulation solely of PV networks produced an increase in the frequency and amplitude of fast GABAergic IPSCs in CA1 pyramidal cells, which could enhance oscillatory power in theta and gamma bands. M_1 mAChR-dependent modulation of PV cells could enhance PING through direct depolarization-dependent and depolarization-independent mechanisms. Future work that examines how M_1 mAChR modulation alters the intrinsic resonance properties (Pike *et al.* 2000) and glutamatergic excitation (Pafundo *et al.* 2013) of HC PV cells would further elucidate this issue.

In addition to M_1 mAChRs on PV cells, mAChRs are expressed on non-PV interneurons, including cannabinoid-sensitive CCK+ interneurons (Neu *et al.* 2007; Cea-del Rio *et al.* 2010; Nagode *et al.* 2011, 2014) and SOM+ interneurons (Lawrence *et al.* 2006*c*). Moreover, presynaptic mAChRs on PV GABAergic terminals (Hájos *et al.* 1998) and glutamatergic terminals (Seeger *et al.* 2004; Levy *et al.* 2008; Dasari & Gulledge, 2011), nicotinic ACh receptors on various types of interneurons (Bell *et al.* 2011; Tang *et al.* 2011; Leão *et al.* 2012), and indirect mechanisms, such as activity-dependent release of endocannabinoids (Neu *et al.* 2007; Péterfi *et al.* 2012) and CCK (Földy *et al.* 2007), would impact the generation and maintenance of cholinergically induced oscillations. Finally, intrinsic mechanisms of short-term plasticity will factor into circuit dynamics (Zucker & Regehr, 2002; Daw *et al.* 2009; Szabó *et al.* 2010; Pafundo *et al.* 2013). Though we do not doubt that the underlying mechanisms of cholinergically induced oscillations involve complex cellular and synaptic interactions across many different HC interneuron subtypes, we do find that activation of M_1 mAChRs induces a major depolarizing drive in HC PV interneurons, thereby providing a postsynaptic mechanism for enhancing the participation of HC PV cells in network activity. Understanding how synaptic ACh release regulates HC and PFC circuit elements will probably require the inclusion of mAChR-mediated mechanisms in computational network models (Cutsuridis *et al.* 2010; Cutsuridis & Hasselmo, 2012).

M_1 muscarinic acetylcholine receptor-mediated modulation of parvalbumin circuits during behavioural learning tasks

HC oscillations in theta and gamma bands are associated with learning and memory (Montgomery & Buzsáki, 2007; Duzel *et al.* 2010) and their interplay may create a neural code for information storage and retrieval (Lisman & Jensen, 2013). Increased ACh levels in the HC and PFC also correlate with learning and memory (Fadda *et al.* 1996; Degroot & Parent, 2000; Hironaka *et al.* 2001; Pepeu & Giovannini, 2004), and modulate the magnitude of HC theta oscillations (Givens & Olton, 1990; Lee *et al.* 1994). Gamma oscillations *in vitro* are enhanced by the activation of M_1 mAChRs (Spencer *et al.* 2010) and impaired in M_1 mAChR KO mice (Fisahn *et al.* 2002). While HC PV interneurons in CA1 participate in theta and gamma oscillations (Klausberger *et al.* 2003; Tukker *et al.* 2007), blockade of HC M_1 mAChRs (Ohno *et al.* 1994) or PV cell function (Murray *et al.* 2011) impairs working memory.

Direct evidence that M_1 mAChRs are the major postsynaptic mAChR subtype on PV BCs (Cea-del Rio *et al.* 2011) led us to investigate whether cholinergic activation of M_1 mAChR on PV cells is important for learning tasks. In the spontaneous alternation T-maze, PV-M_1KO and WT mice performed similarly at 1 s and 30 s intervals, yet an interaction in time was noted for PV-M_1KO mice but not WT mice (Fig. 14*B*). This difference suggests that that synaptically released ACh *in vivo* may activate M_1 mAChRs on PV interneurons during working memory tasks. As working memory is thought to involve the cholinergic activation of both PFC and HC (Hasselmo & Sarter, 2011), the loss of M_1 mAChRs on PV cells from either brain region may contribute to the deficit observed in PV-M_1KO mice. HC PV cells exhibit a larger mAChR-induced depolarization than cortical PV cells (Fig. 5*H* and *I*; Kawaguchi, 1997; Cea-del Rio *et al.* 2010; Chiang *et al.* 2010; Pafundo *et al.* 2013), suggesting that interneuron gamma is a more prominent mechanism in HC than PFC. Gamma oscillations, a signature of PV cell excitation, are detected during working memory tasks (Montgomery & Buzsáki, 2007) and increase during memory load (van Vugt *et al.* 2010). However, the relationships between PV excitability, network oscillations and working memory may be complex because reducing glutamatergic excitation of PV cells impairs working memory without reducing gamma (Korotkova *et al.* 2010) or ripple (Rácz *et al.* 2009) oscillations.

ACh release is increased in both HC and PFC during recognition of novel objects (Acquas *et al.* 1996). We observed an impairment in NOR in PV-M_1KO mice but not WT mice (Fig. 14*E*). Therefore, our results imply that M_1 mAChRs on both PFC and HC PV interneurons are important for NOR. Recent evidence places greater emphasis on the HC than PFC for object recognition memory (Clark, 2013; Cohen *et al.* 2013). Finally, PV-M_1KO mice performed normally in the MWM (Fig. 14*F–J*), consistent with other studies that demonstrate that the disruption of PV interneuron function can lead to selective learning deficits without disrupting reference memory (Fuchs *et al.* 2007; Korotkova *et al.* 2010; Murray *et al.* 2011; Carlén *et al.* 2012). Interestingly, in working memory tasks, a subset of PV-M_1KO mice exhibited a 0% correct choice, indicating that they preferred the familiar arm. Similarly, in the NOR task, PV-M_1KO mice spent more time with the familiar

object. Both of these observations indicate perseveration and a comfort with the familiar, which may indicate cognitive dysfunction suggestive of an autistic (Perry *et al.* 2001; Mukaetova-Ladinska *et al.* 2010) or schizophrenic (Berman *et al.* 2007; Scarr & Dean, 2008; Scarr *et al.* 2013) phenotype.

An impairment of PV-M_1KO mice in working and/or recognition memory suggests that direct cholinergic excitation of local PV neurons, and cholinergically induced oscillations *in vivo*, are critical for these memory tasks. Spatial reference memory may be more reliant on the distributed, collective action of many different cell types, including the M_3 mAChR preferring GABAergic septohippocampal neurons (Alreja *et al.* 2000) and various non-PV HC targets (Buzsáki, 2002; Nagode *et al.* 2011, 2014), perhaps making direct cholinergic modulation of local PV cells less critical to spatial reference memory. Scopolamine administration exacerbates memory deficits in M_1 KO mice (Anagnostaras *et al.* 2003), indicating that additional mAChR subtypes are involved in cholinergically dependent HC learning and memory tasks. M_2 mAChR KO mice exhibit HC learning deficits and have more pronounced disruption of normal inhibitory transmission than excitatory transmission (Seeger *et al.* 2004), possibly indicative of the importance of presynaptic M_2 mAChRs in the regulation of GABA release from PV cell terminals (Hájos *et al.* 1998; Szabó *et al.* 2010). Therefore, postsynaptic M_1 and presynaptic M_2 mAChRs may be synergistically activated on PV cells during cholinergically induced HC oscillations *in vivo*, and their collective action could aid in neuronal synchronization and lower the threshold for long-term potentiation (Ovsepian *et al.* 2004). Future *in vivo* single unit recordings from PV cells during different behavioural tasks would further elucidate the relationships between PV circuit function, oscillatory activity and learning.

Implications for disease states

We have gained insights into the mechanisms by which cholinergic modulation of PV cells contributes to HC function. Inhibitory interneuron (Marín, 2012) and M_1 mAChR dysfunction has been implicated in many disease states, including Alzheimer's disease (German *et al.* 2003; Medeiros *et al.* 2011), schizophrenia (Berman *et al.* 2007; Raedler *et al.* 2007) and epilepsy (Friedman *et al.* 2007). Positive allosteric modulators of M_1 mAChRs promote gamma oscillations (Spencer *et al.* 2010), improve HC-dependent learning (Ragozzino *et al.* 2012; Digby *et al.* 2012) and have been suggested to be an effective treatment strategy for schizophrenia (Scarr & Dean, 2008; Scarr *et al.* 2013). Therefore, M_1 mAChRs on PV cells may be an important therapeutic target in the future.

References

Acquas E, Wilson C & Fibiger HC (1996). Conditioned and unconditioned stimuli increase frontal cortical and hippocampal acetylcholine release: effects of novelty, habituation, and fear. *J Neurosci* **16**, 3089–3096.

Alexander GM, Rogan SC, Abbas AI, Armbruster BN, Pei Y, Allen JA, Nonneman RJ, Hartmann J, Moy SS, Nicolelis MA, McNamara JO & Roth BL (2009). Remote control of neuronal activity in transgenic mice expressing evolved G protein-coupled receptors. *Neuron* **63**, 27–39.

Alreja M, Wu M, Liu W, Atkins JB, Leranth C & Shanabrough M (2000). Muscarinic tone sustains impulse flow in the septohippocampal GABA but not cholinergic pathway: implications for learning and memory. *J Neurosci* **20**, 8103–8110.

Anagnostaras SG, Murphy GG, Hamilton SE, Mitchell SL, Rahnama NP, Nathanson NM & Silva AJ (2003). Selective cognitive dysfunction in acetylcholine M1 muscarinic receptor mutant mice. *Nat Neurosci* **6**, 51–58.

Armbruster BN, Li X, Pausch MH, Herlitze S & Roth BL (2007). Evolving the lock to fit the key to create a family of G protein-coupled receptors potently activated by an inert ligand. *Proc Natl Acad Sci U S A* **104**, 5163–5168.

Atallah BV & Scanziani M (2009). Instantaneous modulation of gamma oscillation frequency by balancing excitation with inhibition. *Neuron* **62**, 566–577.

Atzori M, Lau D, Tansey EP, Chow A, Ozaita A, Rudy B & McBain CJ (2000). H2 histamine receptor-phosphorylation of Kv3.2 modulates interneuron fast spiking. *Nat Neurosci* **3**, 791–798.

Bartos M, Vida I, Frotscher M, Geiger JR & Jonas P (2001). Rapid signaling at inhibitory synapses in a dentate gyrus interneuron network. *J Neurosci* **21**, 2687–2698.

Bartos M, Vida I & Jonas P (2007). Synaptic mechanisms of synchronized gamma oscillations in inhibitory interneuron networks. *Nat Rev Neurosci* **8**, 45–56.

Behrends JC & Bruggencate ten G (1993). Cholinergic modulation of synaptic inhibition in the guinea pig hippocampus in vitro: excitation of GABAergic interneurons and inhibition of GABA-release. *J Neurophysiol* **69**, 626–629.

Bell LA, Bell KA & McQuiston AR (2013). Synaptic muscarinic response types in hippocampal CA1 interneurons depend on different levels of presynaptic activity and different muscarinic receptor subtypes. *Neuropharmacology* **73**, 160–173.

Bell KA, Shim H, Chen C-K & McQuiston AR (2011). Nicotinic excitatory postsynaptic potentials in hippocampal CA1 interneurons are predominantly mediated by nicotinic receptors that contain α4 and β2 subunits. *Neuropharmacology* **61**, 1379–1388.

Berman JA, Talmage DA & Role LW (2007). Cholinergic circuits and signaling in the pathophysiology of schizophrenia. *Int Rev Neurobiol* **78**, 193–223.

Bevins RA & Besheer J (2006). Object recognition in rats and mice: a one-trial non-matching-to-sample learning task to study 'recognition memory'. *Nat Protoc* **1**, 1306–1311.

Bischofberger J, Engel D, Li L, Geiger JRP & Jonas P (2006). Patch-clamp recording from mossy fiber terminals in hippocampal slices. *Nat Protoc* **1**, 2075–2081.

Brito GN, Davis BJ, Stopp LC & Stanton ME (1983). Memory and the septo-hippocampal cholinergic system in the rat. *Psychopharmacology (Berl)* **81**, 315–320.

Buhl EH, Halasy K & Somogyi P (1994). Diverse sources of hippocampal unitary inhibitory postsynaptic potentials and the number of synaptic release sites. *Nature* **368**, 823–828.

Buzsáki G (2002). Theta oscillations in the hippocampus. *Neuron* **33**, 325–340.

Buzsáki G & Wang X-J (2012). Mechanisms of gamma oscillations. *Annu Rev Neurosci* **35**, 203–225.

Cardin JA, Carlén M, Meletis K, Knoblich U, Zhang F, Deisseroth K, Tsai L-H & Moore CI (2009). Driving fast-spiking cells induces gamma rhythm and controls sensory responses. *Nature* **459**, 663–667.

Carlén M, Meletis K, Siegle JH, Cardin JA, Futai K, Vierling-Claassen D, Rühlmann C, Jones SR, Deisseroth K, Sheng M, Moore CI & Tsai L-H (2012). A critical role for NMDA receptors in parvalbumin interneurons for gamma rhythm induction and behavior. *Mol Psychiatry* **17**, 537–548.

Cea-del Rio CA, Lawrence JJ, Tricoire L, Erdelyi F, Szabo G & McBain CJ (2010). M3 muscarinic acetylcholine receptor expression confers differential cholinergic modulation to neurochemically distinct hippocampal basket cell subtypes. *J Neurosci* **30**, 6011–6024.

Cea-del Rio CA, Lawrence JJ, Erdelyi F, Szabo G & McBain CJ (2011). Cholinergic modulation amplifies the intrinsic oscillatory properties of CA1 hippocampal cholecystokinin-positive interneurons. *J Physiol (Lond)* **589**, 609–627.

Cea-del Rio CA, McBain CJ & Pelkey KA (2012). An update on cholinergic regulation of cholecystokinin-expressing basket cells. *J Physiol (Lond)* **590**, 695–702.

Chen Y-J, Zhang M, Yin D-M, Wen L, Ting A, Wang P, Lu Y-S, Zhu X-H, Li S-J, Wu C-Y, Wang X-M, Lai C, Xiong W-C, Mei L & Gao T-M (2010). ErbB4 in parvalbumin-positive interneurons is critical for neuregulin 1 regulation of long-term potentiation. *Proc Natl Acad Sci U S A* **107**, 21818–21823.

Chiang PH, Yeh WC, Lee CT, Weng JY, Huang YY & Lien CC (2010). M_1-like muscarinic acetylcholine receptors regulate fast-spiking interneuron excitability in rat dentate gyrus. *Neuroscience* **169**, 39–51.

Clark RE (2013). Recognition memory: an old idea given new life. *Curr Biol* **23**, R725–R727.

Clements JD & Bekkers JM (1997). Detection of spontaneous synaptic events with an optimally scaled template. *Biophys J* **73**, 220–229.

Cobb S & Lawrence JJ (2010). Neuromodulation of hippocampal cells and circuits. In *Hippocampal Microcircuits. A Computational Modeler's Resource Book*, ed. Cutsuridis V, Graham B, Cobb S & Vida I, pp. 187–246. Springer Series in Computational Neuroscience, New York.

Cohen SJ, Munchow AH, Rios LM, Zhang G, Asgeirsdóttir HN & Stackman RW (2013). The rodent hippocampus is essential for nonspatial object memory. *Curr Biol* **23**, 1685–1690.

Cooper EC, Harrington E, Jan YN & Jan LY (2001). M channel KCNQ2 subunits are localized to key sites for control of neuronal network oscillations and synchronization in mouse brain. *J Neurosci* **21**, 9529–9540.

Coyle JT, Price DL & DeLong MR (1983). Alzheimer's disease: a disorder of cortical cholinergic innervation. *Science* **219**, 1184–1190.

Crawley JN (2007). Motor Functions. In *What's Wrong with my Mouse?*, pp. 63–84. John Wiley & Sons, Inc., Hoboken, NJ.

Crawley JN & Paylor R (1997). A proposed test battery and constellations of specific behavioral paradigms to investigate the behavioral phenotypes of transgenic and knockout mice. *Horm Behav* **31**, 197–211.

Croxson PL, Kyriazis DA & Baxter MG (2011). Cholinergic modulation of a specific memory function of prefrontal cortex. *Nat Neurosci* **14**, 1510–1512.

Cutsuridis V & Hasselmo M (2012). GABAergic contributions to gating, timing, and phase precession of hippocampal neuronal activity during theta oscillations. *Hippocampus* **22**, 1597–1621.

Cutsuridis V, Cobb S & Graham BP (2010). Encoding and retrieval in a model of the hippocampal CA1 microcircuit. *Hippocampus* **20**, 423–446.

Dasari S & Gulledge AT (2011). M1 and M4 receptors modulate hippocampal pyramidal neurons. *J Neurophysiol* **105**, 779–792.

Daw MI, Tricoire L, Erdelyi F, Szabo G & McBain CJ (2009). Asynchronous transmitter release from cholecystokinin-containing inhibitory interneurons is widespread and target-cell independent. *J Neurosci* **29**, 11112–11122.

Deacon RMJ & Rawlins JNP (2006). T-maze alternation in the rodent. *Nat Protoc* **1**, 7–12.

Degroot AA & Parent MBM (2000). Increasing acetylcholine levels in the hippocampus or entorhinal cortex reverses the impairing effects of septal GABA receptor activation on spontaneous alternation. *Learn Mem* **7**, 293–302.

Digby GJ *et al.* (2012). Novel allosteric agonists of M1 muscarinic acetylcholine receptors induce brain region-specific responses that correspond with behavioral effects in animal models. *J Neurosci* **32**, 8532–8544.

Disney AA & Aoki C (2008). Muscarinic acetylcholine receptors in macaque V1 are most frequently expressed by parvalbumin-immunoreactive neurons. *J Comp Neurol* **507**, 1748–1762.

Duzel E, Penny WD & Burgess N (2010). Brain oscillations and memory. *Curr Opin Neurobiol* **20**, 143–149.

Erisir A, Lau D, Rudy B & Leonard CS (1999). Function of specific K^+ channels in sustained high-frequency firing of fast-spiking neocortical interneurons. *J Neurophysiol* **82**, 2476–2489.

Fadda F, Melis F & Stancampiano R (1996). Increased hippocampal acetylcholine release during a working memory task. *Eur J Pharmacol* **307**, R1–R2.

Fellous JM & Sejnowski TJ (2000). Cholinergic induction of oscillations in the hippocampal slice in the slow (0.5–2 Hz), theta (5–12 Hz), and gamma (35–70 Hz) bands. *Hippocampus* **10**, 187–197.

Fisahn A, Pike FG, Buhl EH & Paulsen O (1998). Cholinergic induction of network oscillations at 40 Hz in the hippocampus in vitro. *Nature* **394**, 186–189.

Fisahn A, Yamada M, Duttaroy A, Gan J-W, Deng C-X, McBain CJ & Wess J (2002). Muscarinic induction of hippocampal gamma oscillations requires coupling of the M1 receptor to two mixed cation currents. *Neuron* **33**, 615–624.

Földy C, Lee SY, Szabadics J, Neu A & Soltesz I (2007). Cell type-specific gating of perisomatic inhibition by cholecystokinin. *Nat Neurosci* **10**, 1128–1130.

Fraser DD & MacVicar BA (1996). Cholinergic-dependent plateau potential in hippocampal CA1 pyramidal neurons. *J Neurosci* **16**, 4113–4128.

Freund TF & Buzsáki GY (1996). Interneurons of the hippocampus. *Hippocampus* **6**, 347–470.

Freund TF & Katona I (2007). Perisomatic inhibition. *Neuron* **56**, 33–42.

Friedman A, Behrens CJ & Heinemann U (2007). Cholinergic dysfunction in temporal lobe epilepsy. *Epilepsia* **48**(Suppl 5), 126–130.

Fuchs EC, Zivkovic AR, Cunningham MO, Middleton S, Lebeau FEN, Bannerman DM, Rozov A, Whittington MA, Traub RD, Rawlins JNP & Monyer H (2007). Recruitment of parvalbumin-positive interneurons determines hippocampal function and associated behavior. *Neuron* **53**, 591–604.

Geiger JRP, Bischofberger J, Vida I, Fröbe U, Pfitzinger S, Weber HJ, Haverkampf K & Jonas P (2002). Patch-clamp recording in brain slices with improved slicer technology. *Pflugers Arch* **443**, 491–501.

Geiger J, Weber YG, Landwehrmeyer B, Sommer C & Lerche H (2006). Immunohistochemical analysis of KCNQ3 potassium channels in mouse brain. *Neurosci Lett* **400**, 101–104.

Gerber DJ, Sotnikova TD, Gainetdinov RR, Huang SY, Caron MG & Tonegawa S (2001). Hyperactivity, elevated dopaminergic transmission, and response to amphetamine in M1 muscarinic acetylcholine receptor-deficient mice. *Proc Natl Acad Sci U S A* **98**, 15312–15317.

German DC, Yazdani U, Speciale SG, Pasbakhsh P, Games D & Liang C-L (2003). Cholinergic neuropathology in a mouse model of Alzheimer's disease. *J Comp Neurol* **462**, 371–381.

Givens BS & Olton DS (1990). Cholinergic and GABAergic modulation of medial septal area: effect on working memory. *Behav Neurosci* **104**, 849–855.

Glickfeld LL & Scanziani M (2006). Distinct timing in the activity of cannabinoid-sensitive and cannabinoid-insensitive basket cells. *Nat Neurosci* **9**, 807–815.

Gloveli T, Dugladze T, Saha S, Monyer H, Heinemann U, Traub RD, Whittington MA & Buhl EH (2005). Differential involvement of oriens/pyramidale interneurones in hippocampal network oscillations in vitro. *J Physiol (Lond)* **562**, 131–147.

Gulledge AT, Park SB, Kawaguchi Y & Stuart GJ (2007). Heterogeneity of phasic cholinergic signaling in neocortical neurons. *J Neurophysiol* **97**, 2215–2229.

Gulyás AI, Megías M, Emri Z & Freund TF (1999). Total number and ratio of excitatory and inhibitory synapses converging onto single interneurons of different types in the CA1 area of the rat hippocampus. *J Neurosci* **19**, 10082–10097.

Gulyás AI, Szabó GG, Ulbert I, Holderith N, Monyer H, Erdelyi F, Szabo G, Freund TF & Hájos N (2010). Parvalbumin-containing fast-spiking basket cells generate the field potential oscillations induced by cholinergic receptor activation in the hippocampus. *J Neurosci* **30**, 15134–15145.

Hájos N, Papp EC, Acsády L, Levey AI & Freund TF (1998). Distinct interneuron types express m2 muscarinic receptor immunoreactivity on their dendrites or axon terminals in the hippocampus. *Neuroscience* **82**, 355–376.

Hamilton SE, Loose MD, Qi M, Levey AI, Hille B, McKnight GS, Idzerda RL & Nathanson NM (1997). Disruption of the m1 receptor gene ablates muscarinic receptor-dependent M current regulation and seizure activity in mice. *Proc Natl Acad Sci U S A* **94**, 13311–13316.

Hasselmo ME & Sarter M (2011). Modes and models of forebrain cholinergic neuromodulation of cognition. *Neuropsychopharmacology* **36**, 52–73.

Hefft S, Kraushaar U, Geiger JRP & Jonas P (2002). Presynaptic short-term depression is maintained during regulation of transmitter release at a GABAergic synapse in rat hippocampus. *J Physiol (Lond)* **539**, 201–208.

Henze DA, Borhegyi Z, Csicsvari J, Mamiya A, Harris KD & Buzsáki G (2000). Intracellular features predicted by extracellular recordings in the hippocampus in vivo. *J Neurophysiol* **84**, 390–400.

Hippenmeyer S, Vrieseling E, Sigrist M, Portmann T, Laengle C, Ladle DR & Arber S (2005). A developmental switch in the response of DRG neurons to ETS transcription factor signaling. *PLoS Biol* **3**, e159.

Hironaka N, Tanaka K, Izaki Y, Hori K & Nomura M (2001). Memory-related acetylcholine efflux from rat prefrontal cortex and hippocampus: a microdialysis study. *Brain Res* **901**, 143–150.

Kamsler A, McHugh TJ, Gerber D, Huang SY & Tonegawa S (2010). Presynaptic m1 muscarinic receptors are necessary for mGluR long-term depression in the hippocampus. *Proc Natl Acad Sci U S A* **107**, 1618–1623.

Kawaguchi Y (1997). Selective cholinergic modulation of cortical GABAergic cell subtypes. *J Neurophysiol* **78**, 1743–1747.

Klausberger T (2009). GABAergic interneurons targeting dendrites of pyramidal cells in the CA1 area of the hippocampus. *Eur J Neurosci* **30**, 947–957.

Klausberger T & Somogyi P (2008). Neuronal diversity and temporal dynamics: the unity of hippocampal circuit operations. *Science* **321**, 53–57.

Klausberger T, Magill PJ, Márton LF, Roberts JDB, Cobden PM, Buzsáki G & Somogyi P (2003). Brain-state- and cell-type-specific firing of hippocampal interneurons in vivo. *Nature* **421**, 844–848.

Korotkova T, Fuchs EC, Ponomarenko A, Engelhardt von J & Monyer H (2010). NMDA receptor ablation on parvalbumin-positive interneurons impairs hippocampal synchrony, spatial representations, and working memory. *Neuron* **68**, 557–569.

Krashes MJ, Koda S, Ye C, Rogan SC, Adams AC, Cusher DS, Maratos-Flier E, Roth BL & Lowell BB (2011). Rapid, reversible activation of AgRP neurons drives feeding behavior in mice. *J Clin Invest* **121**, 1424–1428.

Kuhlman SJ & Huang ZJ (2008). High-resolution labeling and functional manipulation of specific neuron types in mouse brain by Cre-activated viral gene expression. *PLoS ONE* **3**, e2005.

Lawrence JJ (2010). Subcortical neuromodulation of feedforward and feedback inhibitory microcircuits by the reticular activating system. In *GABA and Sleep: Molecular, Functional and Clinical Aspects*, ed. Monti JM, Pandi-Perumal SR, Möhler H, p. 147. Springer, Basel147.

Lawrence JJ, Grinspan ZM & McBain CJ (2004). Quantal transmission at mossy fibre targets in the CA3 region of the rat hippocampus. *J Physiol (Lond)* **554**, 175–193.

Lawrence JJ, Grinspan ZM, Statland JM & McBain CJ (2006*a*). Muscarinic receptor activation tunes mouse stratum oriens interneurones to amplify spike reliability. *J Physiol (Lond)* **571**, 555–562.

Lawrence JJ, Saraga F, Churchill JF, Statland JM, Travis KE, Skinner FK & McBain CJ (2006*b*). Somatodendritic Kv7/KCNQ/M channels control interspike interval in hippocampal interneurons. *J Neurosci* **26**, 12325–12338.

Lawrence JJ, Statland JM, Grinspan ZM & McBain CJ (2006*c*). Cell type-specific dependence of muscarinic signalling in mouse hippocampal stratum oriens interneurones. *J Physiol (Lond)* **570**, 595–610.

Leão RN, Mikulovic S, Leão KE, Munguba H, Gezelius H, Enjin A, Patra K, Eriksson A, Loew LM, Tort ABL & Kullander K (2012). OLM interneurons differentially modulate CA3 and entorhinal inputs to hippocampal CA1 neurons. *Nat Neurosci* **15**, 1524–1530.

Lee MG, Chrobak JJ, Sik A, Wiley RG & Buzsáki G (1994). Hippocampal theta activity following selective lesion of the septal cholinergic system. *Neuroscience* **62**, 1033–1047.

Levy RB, Reyes AD & Aoki C (2008). Cholinergic modulation of local pyramid-interneuron synapses exhibiting divergent short-term dynamics in rat sensory cortex. *Brain Res* **1215**, 97–104.

Lien C-C & Jonas P (2003). Kv3 potassium conductance is necessary and kinetically optimized for high-frequency action potential generation in hippocampal interneurons. *J Neurosci* **23**, 2058–2068.

Lisman JE & Jensen O (2013). The theta-gamma neural code. *Neuron* **77**, 1002–1016.

Maccaferri G, Roberts JD, Szucs P, Cottingham CA & Somogyi P (2000). Cell surface domain specific postsynaptic currents evoked by identified GABAergic neurones in rat hippocampus in vitro. *J Physiol (Lond)* **524**(Pt 1), 91–116.

Madisen L, Zwingman TA, Sunkin SM, Oh SW, Zariwala HA, Gu H, Ng LL, Palmiter RD, Hawrylycz MJ, Jones AR, Lein ES & Zeng H (2009). A robust and high-throughput Cre reporting and characterization system for the whole mouse brain. *Nat Neurosci* **13**, 133–140.

Marín O (2012). Interneuron dysfunction in psychiatric disorders. *Nat Rev Neurosci* **13**, 107–120.

McBain CJ, DiChiara TJ & Kauer JA (1994). Activation of metabotropic glutamate receptors differentially affects two classes of hippocampal interneurons and potentiates excitatory synaptic transmission. *J Neurosci* **14**, 4433–4445.

McCormick DA & Prince DA (1985). Two types of muscarinic response to acetylcholine in mammalian cortical neurons. *Proc Natl Acad Sci U S A* **82**, 6344–6348.

Medeiros R, Kitazawa M, Caccamo A, Baglietto-Vargas D, Estrada-Hernandez T, Cribbs DH, Fisher A & LaFerla FM (2011). Loss of muscarinic M1 receptor exacerbates Alzheimer's disease-like pathology and cognitive decline. *Am J Pathol* **179**, 980–991.

Miyakawa T, Yamada M, Duttaroy A & Wess J (2001). Hyperactivity and intact hippocampus-dependent learning in mice lacking the M1 muscarinic acetylcholine receptor. *J Neurosci* **21**, 5239–5250.

Montgomery SM & Buzsáki G (2007). Gamma oscillations dynamically couple hippocampal CA3 and CA1 regions during memory task performance. *Proc Natl Acad Sci U S A* **104**, 14495–14500.

Mukaetova-Ladinska EB, Westwood J & Perry EK (2010). Cholinergic component of autism spectrum disorder. In *The Neurochemical Basis of Autism: From Molecules to Minicolumns*, ed. Blatt GJ, pp. 129–161. Springer.

Murray AJ, Sauer J-F, Riedel G, McClure C, Ansel L, Cheyne L, Bartos M, Wisden W & Wulff P (2011). Parvalbumin-positive CA1 interneurons are required for spatial working but not for reference memory. *Nat Neurosci* **14**, 297–299.

Nagode DA, Tang A-H, Karson MA, Klugmann M & Alger BE (2011). Optogenetic release of ACh induces rhythmic bursts of perisomatic IPSCs in hippocampus. *PLoS ONE* **6**, e27691.

Nagode DA, Tang A-H, Yang K & Alger BE (2014). Optogenetic identification of an intrinsic cholinergically driven inhibitory oscillator sensitive to cannabinoids and opioids in hippocampal CA1. *J Physiol (Lond)* **592**, 103–123.

Neu A, Földy C & Soltesz I (2007). Postsynaptic origin of CB1-dependent tonic inhibition of GABA release at cholecystokinin-positive basket cell to pyramidal cell synapses in the CA1 region of the rat hippocampus. *J Physiol (Lond)* **578**, 233–247.

Ohno M, Yamamoto T & Watanabe S (1994). Blockade of hippocampal M1 muscarinic receptors impairs working memory performance of rats. *Brain Res* **650**, 260–266.

Oren I, Hájos N & Paulsen O (2010). Identification of the current generator underlying cholinergically induced gamma frequency field potential oscillations in the hippocampal CA3 region. *J Physiol (Lond)* **588**, 785–797.

Ovsepian SV, Anwyl R & Rowan MJ (2004). Endogenous acetylcholine lowers the threshold for long-term potentiation induction in the CA1 area through muscarinic receptor activation: in vivo study. *Eur J Neurosci* **20**, 1267–1275.

Pafundo DE, Miyamae T, Lewis DA & Gonzalez-Burgos G (2013). Cholinergic modulation of neuronal excitability and recurrent excitation-inhibition in prefrontal cortex circuits: implications for gamma oscillations. *J Physiol (Lond)* **591**, 4725–4748.

Pepeu G & Giovannini MG (2004). Changes in acetylcholine extracellular levels during cognitive processes. *Learn Mem* **11**, 21–27.

Perry EK, Lee ML, Martin-Ruiz CM, Court JA, Volsen SG, Merrit J, Folly E, Iversen PE, Bauman ML, Perry RH & Wenk GL (2001). Cholinergic activity in autism: abnormalities in the cerebral cortex and basal forebrain. *Am J Psychiatry* **158**, 1058–1066.

Péterfi Z, Urbán GM, Papp OI, Németh B, Monyer H, Szabo G, Erdelyi F, Mackie K, Freund TF, Hájos N & Katona I (2012). Endocannabinoid-mediated long-term depression of afferent excitatory synapses in hippocampal pyramidal cells and GABAergic interneurons. *J Neurosci* **32**, 14448–14463.

Pike FG, Goddard RS, Suckling JM, Ganter P, Kasthuri N & Paulsen O (2000). Distinct frequency preferences of different types of rat hippocampal neurones in response to oscillatory input currents. *J Physiol (Lond)* **529**(Pt 1), 205–213.

Pitler TA & Alger BE (1992). Cholinergic excitation of GABAergic interneurons in the rat hippocampal slice. *J Physiol (Lond)* **450**, 127–142.

Pouille F & Scanziani M (2004). Routing of spike series by dynamic circuits in the hippocampus. *Nature* **429**, 717–723.

Raedler TJ, Bymaster FP, Tandon R, Copolov D & Dean B (2007). Towards a muscarinic hypothesis of schizophrenia. *Mol Psychiatry* **12**, 232–246.

Ragozzino ME, Artis S, Singh A, Twose TM, Beck JE & Messer WS (2012). The selective M1 muscarinic cholinergic agonist CDD-0102A enhances working memory and cognitive flexibility. *J Pharmacol Exp Ther* **340**, 588–594.

Rácz A, Ponomarenko AA, Fuchs EC & Monyer H (2009). Augmented hippocampal ripple oscillations in mice with reduced fast excitation onto parvalbumin-positive cells. *J Neurosci* **29**, 2563–2568.

Reich CG, Karson MA, Karnup SV, Jones LM & Alger BE (2005). Regulation of IPSP theta rhythm by muscarinic receptors and endocannabinoids in hippocampus. *J Neurophysiol* **94**, 4290–4299.

Ribak CE, Vaughn JE & Saito K (1978). Immunocytochemical localization of glutamic acid decarboxylase in neuronal somata following colchicine inhibition of axonal transport. *Brain Res* **140**, 315–332.

Rouse ST, Hamilton SE, Potter LT, Nathanson NM & Conn PJ (2000). Muscarinic-induced modulation of potassium conductances is unchanged in mouse hippocampal pyramidal cells that lack functional M1 receptors. *Neurosci Lett* **278**, 61–64.

Rudy B & McBain CJ (2001). Kv3 channels: voltage-gated K^+ channels designed for high-frequency repetitive firing. *Trends Neurosci* **24**, 517–526.

Scarr E & Dean B (2008). Muscarinic receptors: do they have a role in the pathology and treatment of schizophrenia? *J Neurochem* **107**, 1188–1195.

Scarr E, Gibbons AS, Neo J, Udawela M & Dean B (2013). Cholinergic connectivity: it's implications for psychiatric disorders. *Front Cell Neurosci* **7**, 55.

Seeger T, Fedorova I, Zheng F, Miyakawa T, Koustova E, Gomeza J, Basile AS, Alzheimer C & Wess J (2004). M2 muscarinic acetylcholine receptor knock-out mice show deficits in behavioral flexibility, working memory, and hippocampal plasticity. *J Neurosci* **24**, 10117–10127.

Sik A, Penttonen M, Ylinen A & Buzsáki G (1995). Hippocampal CA1 interneurons: an in vivo intracellular labeling study. *J Neurosci* **15**, 6651–6665.

Sohal VS, Zhang F, Yizhar O & Deisseroth K (2009). Parvalbumin neurons and gamma rhythms enhance cortical circuit performance. *Nature* **459**, 698–702.

Soriano P (1999). Generalized lacZ expression with the ROSA26 Cre reporter strain. *Nat Genet* **21**, 70–71.

Spencer JP, Middleton LJ & Davies CH (2010). Investigation into the efficacy of the acetylcholinesterase inhibitor, donepezil, and novel procognitive agents to induce gamma oscillations in rat hippocampal slices. *Neuropharmacology* **59**, 437–443.

Srinivas S, Watanabe T, Lin CS, William CM, Tanabe Y, Jessell TM & Costantini F (2001). Cre reporter strains produced by targeted insertion of EYFP and ECFP into the ROSA26 locus. *BMC Dev Biol* **1**, 4.

Szabó GG, Holderith N, Gulyás AI, Freund TF & Hájos N (2010). Distinct synaptic properties of perisomatic inhibitory cell types and their different modulation by cholinergic receptor activation in the CA3 region of the mouse hippocampus. *Eur J Neurosci* **31**, 2234–2246.

Tang A-H, Karson MA, Nagode DA, McIntosh JM, Uebele VN, Renger JJ, Klugmann M, Milner TA & Alger BE (2011). Nerve terminal nicotinic acetylcholine receptors initiate quantal GABA release from perisomatic interneurons by activating axonal T-type (Cav3) Ca^{2+} channels and Ca^{2+} release from stores. *J Neurosci* **31**, 13546–13561.

Taniguchi H, He M, Wu P, Kim S, Paik R, Sugino K, Kvitsiani D, Kvitsani D, Fu Y, Lu J, Lin Y, Miyoshi G, Shima Y, Fishell G, Nelson SB & Huang ZJ (2011). A resource of Cre driver lines for genetic targeting of GABAergic neurons in cerebral cortex. *Neuron* **71**, 995–1013.

Tepper JM, Tecuapetla F, Koós T & Ibáñez-Sandoval O (2010). Heterogeneity and diversity of striatal GABAergic interneurons. *Front Neuroanat* **4**, 150.

Tesson L, Heslan J-M, Ménoret S & Anegon I (2002). Rapid and accurate determination of zygosity in transgenic animals by real-time quantitative PCR. *Transgenic Res* **11**, 43–48.

Tukker JJ, Fuentealba P, Hartwich K, Somogyi P & Klausberger T (2007). Cell type-specific tuning of hippocampal interneuron firing during gamma oscillations in vivo. *J Neurosci* **27**, 8184–8189.

van Hooft JA, Giuffrida R, Blatow M & Monyer H (2000). Differential expression of group I metabotropic glutamate receptors in functionally distinct hippocampal interneurons. *J Neurosci* **20**, 3544–3551.

van Vugt MK, Schulze-Bonhage A, Litt B, Brandt A & Kahana MJ (2010). Hippocampal gamma oscillations increase with memory load. *J Neurosci* **30**, 2694–2699.

Vorhees CV & Williams MT (2006). Morris water maze: procedures for assessing spatial and related forms of learning and memory. *Nat Protoc* **1**, 848–858.

Wen L, Lu Y-S, Zhu X-H, Li X-M, Woo R-S, Chen Y-J, Yin D-M, Lai C, Terry AV, Vazdarjanova A, Xiong W-C & Mei L (2010). Neuregulin 1 regulates pyramidal neuron activity via ErbB4 in parvalbumin-positive interneurons. *Proc Natl Acad Sci U S A* **107**, 1211–1216.

Widmer H, Ferrigan L, Davies CH & Cobb SR (2006). Evoked slow muscarinic acetylcholinergic synaptic potentials in rat hippocampal interneurons. *Hippocampus* **16**, 617–628.

Williams JH & Kauer JA (1997). Properties of carbachol-induced oscillatory activity in rat hippocampus. *J Neurophysiol* **78**, 2631–2640.

Yamasaki M, Matsui M & Watanabe M (2010). Preferential localization of muscarinic M1 receptor on dendritic shaft and spine of cortical pyramidal cells and its anatomical evidence for volume transmission. *J Neurosci* **30**, 4408–4418.

Zhang L & McBain CJ (1995). Potassium conductances underlying repolarization and after-hyperpolarization in rat CA1 hippocampal interneurones. *J Physiol (Lond)* **488**(Pt 3), 661–672.

Zucker RS & Regehr WG (2002). Short-term synaptic plasticity. *Annu Rev Physiol* **64**, 355–405.

Additional information

Competing interests

The authors declare no competing financial interests.

Author contributions

All experiments were performed in the laboratory of J.J.L. J.J.L., F.Y., J.B., K.E.S., V.C.S., S.M.M., J.L.P., B.B.H. and A.D.J. designed the experiments and performed the research; F.Y., J.B., K.E.S., S.M.M., J.L.P., B.B.H. and J.J.L. analysed the data; N.M.N. generated global M_1 KO mice; K.D. provided AAVs; D.J.G. and S.T. generated floxed M_1 mice. F.Y., J.B., K.E.S., S.M.M., V.C.S. and J.J.L. wrote the paper. All co-authors have read and approved the final version.

Funding

We are grateful for financial support from National Institutes of Health grant R01 NS069689 (J.J.L.), National Center for Research Resources grant P20RR015583 (J.J.L., J.B. and V.C.S.), the Epilepsy Foundation (J.J.L.), the Alzheimer's Association (J.J.L.), NSF EPSCOR (K.E.S.), the University of Montana Small Grants Program (J.J.L. and K.E.S.) and the Montana Space Grant Consortium (S.M.M.). AnyMaze equipment was purchased with a COBRE CSFN Pilot Grant to Loretta Bolyard (P20RR015583), a Montana Space Grant Consortium grant (S.M.M.) and NSF EPSCOR (K.E.S.). P20RR015583, P20RR017670 and P20GM10356 grants supported core facilities.

Acknowledgements

We thank Miriam Rose Baker and Akua Karikari for assistance with behavioural experiments, Alison Hixon, Brandon Willis and Corbin Schwanke for assistance in genotyping, Ed Calloway (Salk Institute) and Silvia Arber (University of Basel, Switzerland) for PV-CRE mice, Z. Josh Huang (Cold Spring Harbor, NY) and Massimo Scanziani (UCSD) for SOM-CRE mice, Jesse Adams for AxographX event detection programming, Bryan Roth, Dan Urban and Georgia Alexander for advice on the DREADD AAV, David Bonislawski and Weinan Sun for technical advice on stereotaxic injections and confocal imaging, and Ken Pelkey for critically evaluating an earlier version of the manuscript.